12-2011

Paired positive carbonate carbon isotope, organic carbon isotope, and oxygen isotope composition study across the Lower Mississippian positive carbon isotope excursion, southeastern Nevada, USA

Robert Alan Henry
University of Nevada, Las Vegas

PAIRED $\delta^{13}C_{CARB}$, $\delta^{13}C_{ORG}$, AND $\delta^{18}O$ STUDY ACROSS THE LOWER MISSISSIPPIAN POSITIVE CARBON ISOTOPE EXCURSION, SOUTHEASTERN NEVADA, USA

by

Robert Alan Henry

Bachelor of Arts
Hartwick College
2007

A thesis submitted in partial fulfillment of
the requirements for the

Master of Science in Geoscience

Department of Geoscience
College of Science
The Graduate College

University of Nevada, Las Vegas
December 2011

THE GRADUATE COLLEGE

We recommend the thesis prepared under our supervision by

Robert Henry

entitled

Paired $\delta^{13}C_{CARB}$, $\delta^{13}C_{ORG}$, and $\delta^{18}O$ Study Across the Lower Mississippian Positive Carbon Isotope Excursion, Southeastern Nevada, USA

be accepted in partial fulfillment of the requirements for the degree of

Doctor of Science in Geoscience
Department of Geoscience

Ganqing Jiang, Committee Chair

Stephen Rowland, Committee Member

Margaret Rees, Committee Member

Brian Hedlund, Graduate College Representative

Ronald Smith, Ph. D., Vice President for Research and Graduate Studies
and Dean of the Graduate College

December 2011

ABSTRACT

PAIRED $\delta^{13}C_{CARB}$, $\delta^{13}C_{ORG}$, AND $\delta^{18}O$ STUDY ACROSS THE LOWER MISSISSIPPIAN POSITIVE CARBON ISOTOPE EXCURSION, SOUTHEASTERN NEVADA, USA

by

Robert Alan Henry

Dr. Ganqing Jiang, Examination Committee Chair
Associate Professor of Geoscience
University of Nevada, Las Vegas

A prominent positive carbonate carbon isotope ($\delta^{13}C_{carb}$) excursion of Early Mississippian age (ca 351 Ma) has been documented by previous studies from numerous sites globally. This $\delta^{13}C_{carb}$ excursion has been interpreted as resulting from enhanced organic carbon burial that removed ^{13}C-depleted carbon from the ocean and atmosphere. Anticipated outcomes from enhanced organic carbon burial would include a similar positive excursion in organic carbon isotopes ($\delta^{13}C_{org}$) and a global cooling event resulting from reduced CO_2 in the atmosphere and ocean. These predictions, however, were not tested sufficiently in previous studies. This research has tested these predictions through an integrated study of carbonate, and organic carbon, and oxygen isotopes in two Lower Mississippian stratigraphic sections in southeastern Nevada: the Alamo section and the Tungsten Gap section.

Paired $\delta^{13}C_{org}$ and $\delta^{13}C_{carb}$ analyses and brachiopod oxygen isotope analysis across the positive $\delta^{13}C_{carb}$ excursion show that (1) $\delta^{13}C_{carb}$ and $\delta^{13}C_{org}$ values are coupled in the Alamo section, but considerable variations in both $\delta^{13}C_{carb}$ and $\delta^{13}C_{org}$ values are present in the Tungsten Gap section; (2) $\delta^{18}O$ values of limestone matrix and brachiopods show an overall increase across the $\delta^{13}C$ excursion, but increase in $\delta^{18}O$ predates the $\delta^{13}C$

maximum. A significant negative shift in $\delta^{18}O$ from -5‰ to -21‰ is observed before the $\delta^{13}C$ peak; and (3) carbonate and organic carbon isotope fractionation, approximated by the isotope difference ($\Delta\delta^{13}C$) between $\delta^{13}C_{carb}$ and $\delta^{13}C_{org}$ ($\Delta\delta^{13}C = \delta^{13}C_{carb} - \delta^{13}C_{org}$) increases from 26‰ to 31‰ before the $\delta^{13}C$ peak, but remains about 31‰ for the remainder of the excursion interval.

Overall, the data support enhanced organic production and burial as the origin of the $\delta^{13}C$ excursion, but the cooling event occurred earlier than the peak of the carbon isotope excursion. The lack of change in both $\delta^{18}O$ and $\Delta\delta^{13}C$ across the later half of $\delta^{13}C$ excursion suggests that, after the initial cooling at the beginning of the $\delta^{13}C$ excursion, seawater temperature and aqueous CO_2 concentration did not change significantly. Unresolved is the cause of isotopic difference between the Alamo and Tungsten Gap sections. More scattered and lower values in $\delta^{13}C_{carb}$, $\delta^{13}C_{org}$, and $\delta^{18}O$ from the Tungsten Gap section may imply a significant influence from terrestrial sediment sources or freshwater input, but considering the paleogeographic location of section, the later is more likely. Further elucidating the isotope difference between sections requires higher sampling resolution from the Tungsten Gap section and from other sections further eastward in proximal environments of the early Mississippian carbonate platform.

ACKNOWLEDGEMENTS

The completion of this thesis would not have been possible without the work, time, teaching, and support from a large number of people. First and foremost, I would like to thank my advisor Dr. Ganqing Jiang for guiding me in this study and especially in the last year where conditions out of anyone's control made it difficult to focus on getting this work completed. This thesis would not have been possible without the countless hours of guidance from Dr. Jiang. I would also like to thank my committee members, Dr. Stephen Rowland, Dr. Margaret (Peg) Rees, and Dr. Brian Hedlund for helpful insights into my understanding of how to complete this thesis. Additional helpful field insight, brachiopod separation, trace element data and financial support from Dr. Uwe Brand were of great importance to this study. Also, I would like to thank the entire Geoscience faculty that I have had the opportunity to expand my knowledge from over the past few years along with the staff (especially Maria) for putting up with my antics. The support, encouragement, and help in all areas of life from my fellow classmates at UNLV were vital to completing this study. Special thanks to: James, Laura, Swapan, Josh, Aubrey, Nate, Yuki, Jeevan, Adam, Ratna, Jon, Steven, Andy, Jason, Eden. All I can say is thank you, though I don't think that is enough. Also, I would like to thank Dr. Eric Johnson, Dr. Robert Titus, Dr. David Griffing, Dr. Meredith Newman, and the rest of the geology department at Hartwick College for initially cultivating my understanding of geology. Finally, I would like to thank Jim King and ZIA Geological for welcoming me back to work around working on this thesis.

This thesis would not have been possible without generous funding from the department of Geoscience at UNLV, Dr. Ganqing Jiang, and Dr. Uwe Brand. Special

thanks to Cathy Willy for helpful assistance in getting permits for field work with the Bureau of Land Management. I would also like to thank Million Hailemichael for assistance in the preparation and examination of organic carbon samples.

Finally, I want to dedicate this thesis to my friends and family who have always supported my decisions without question especially Katie and Papa who were not able to see the conclusion of this work. Mom, Dad, Grammy, and Mama, thank you for the support and encouragement when life was not going as planned; I could not have done this without you.

TABLE OF CONTENTS

LIST OF FIGURES

CHAPTER 1

INTRODUCTION

Throughout the Phanerozoic, major perturbations of the global carbon cycle are recorded by both positive and negative inorganic carbon isotope ($\delta^{13}C_{carb}$) excursions in stratigraphic successions of North America, Europe, and Asia. Positive $\delta^{13}C_{carb}$ excursions have been interpreted as resulting from an increase in organic carbon burial while negative $\delta^{13}C_{carb}$ excursions are usually thought to be the result of reduced primary organic production (Kump and Arthur, 1999; Hoefs, 2009). If positive $\delta^{13}C_{carb}$ excursions are a direct result of enhanced organic carbon burial, then it is expected that a similar positive excursion in organic carbon isotope ($\delta^{13}C_{org}$) is associated with each $\delta^{13}C_{carb}$ excursion (e.g., Kump and Arthur, 1999). Unlike the $\delta^{13}C_{carb}$ that records the isotope signature of dissolved inorganic carbon (DIC) in the ocean, $\delta^{13}C_{org}$ records the isotope signature of organic matter produced by primary or secondary producers that use dissolved CO_2 in seawater as their carbon source (Hayes et al., 1999). Thus, the $\delta^{13}C_{org}$ values record information on both the $\delta^{13}C$ of the oceanic DIC and isotopic fractionation during carbon fixation. While the latter may cause significant changes in $\delta^{13}C_{org}$ at local to regional scales (e.g., Kump and Arthur, 1999; Hayes et al., 1999; Cramer and Saltzman, 2007; Young et al., 2008), most Phanerozoic $\delta^{13}C_{carb}$ excursions are accompanied with comparable excursions in $\delta^{13}C_{org}$. Typical examples include the Permian-Triassic boundary (Magaritz et al., 1992; Wang et al., 1994; Ward et al., 2005), the Early Jurassic Toarcian anomaly (Hesselbo et al., 2000; 2007; Kemp et al., 2005; Cohen et al., 2007), the Cretaceous ocean anoxic events (Jenkyns, 2003), and the Paleocene-Eocene Thermal Maximum (Pagani et al., 2006; Sluijs et al., 2006; Cohen et

al., 2007). This phenomenon suggests that, at a broader scale, the $\delta^{13}C$ of DIC has first-order control on the secular $\delta^{13}C_{org}$ changes (Hayes et al., 1999) and $\delta^{13}C_{carb}$–$\delta^{13}C_{org}$ covariance is expected in stratigraphic successions.

If positive $\delta^{13}C_{carb}$ excursions are accompanied by similar positive $\delta^{13}C_{org}$ excursions and they were formed by enhanced organic carbon burial, then atmospheric CO_2 level would drop during or after the carbon cycle perturbation. This drop occurs because for each mole of organic carbon buried, one mole of CO_2 is removed from seawater, and consequently from atmosphere because aqueous CO_2 in surface ocean seawater is in equilibrium with atmospheric CO_2. Thus an anticipated outcome from enhanced organic carbon burial would be a global cooling event across each positive $\delta^{13}C$ excursion. Such cooling events should be recorded by oxygen isotope ($\delta^{18}O$) values because global cooling leads to the expansion of polar ice sheets that have low $\delta^{18}O$ values (-30‰ to -50‰), resulting in high $\delta^{18}O$ values in seawater (Alley and Cuffey, 2001). Also anticipated is the change in photosynthetic isotope fractionation that should be recorded in $\Delta\delta^{13}C$ ($\Delta\delta^{13}C=\delta^{13}C_{carb}-\delta^{13}C_{org}$) because lower seawater (atmosphere) CO_2 concentration commonly results in lower carbon isotope fractionation (Hayes et al., 1999; Cramer and Saltzman, 2007).

These predictions, however, have not been adequately tested across the major Phanerozoic $\delta^{13}C$ excursions. In this research, an integrated $\delta^{13}C_{carb}$, $\delta^{13}C_{org}$, and $\delta^{18}O$ analysis across the Tournaisian (Early Mississippian) $\delta^{13}C_{carb}$ excursion is conducted to test the relationship between isotope changes, organic carbon burial, and seawater temperature change. The Tournaisian $\delta^{13}C_{carb}$ excursion is one of the most prominent Paleozoic $\delta^{13}C_{carb}$ excursions (Saltzman et al., 2005) that has been documented in

numerous areas around the globe (Saltzman et al., 2000; Saltzman, 2002; Mii et al., 1999; Buggisch et al., 2008; Bruckshen and Veizer, 1997), but no detailed investigation on the coupling of $\delta^{13}C_{carb}$, $\delta^{13}C_{org}$, and $\delta^{18}O$ has been published, particularly for the sections well-exposed in southeastern Nevada. The objectives of this study are to test (1) whether the $\delta^{13}C_{org}$ shows a similar positive excursion as has been documented in $\delta^{13}C_{carb}$, (2) whether seawater temperature changes across the $\delta^{13}C_{carb}$ excursion, as potentially recorded in oxygen isotopes of well-preserved brachiopods, and (3) whether there is temperature-dependent carbonate and organic carbon isotope fractionation is recorded across the excursion.

CHAPTER 2

GEOLOGIC BACKGROUND

2.1 Location of field areas

Two Lower Mississippian sections were chosen for this study (Figure 1). Both of them are well exposed, and have documented a positive $\delta^{13}C_{carb}$ excursion. The first section is located in the Pahranagat Range near Alamo, Nevada, from which previous studies have reported a Tournaisian positive $\delta^{13}C_{carb}$ excursion (Saltzman et al., 2000; Saltzman, 2002; Buggisch et al., 2008). The second section is in the Tungsten Gap of the Arrow Canyon Range, southeastern Nevada. Carbonate carbon isotope analyses from this section (Saltzman, 2003a) demonstrated a positive $\delta^{13}C_{carb}$ excursion similar to that of the Alamo section. Guided by the results from previous studies, sampling was conducted to cover the entire $\delta^{13}C_{carb}$ excursion at a higher sample resolution, particularly through intervals with large data gaps in previous studies.

2.2 Depositional Setting, Biostratigraphy and Stratigraphic Nomenclature

From Late Devonian (Frasnian) to Early Mississippian (Tournaisian or Kinderhookian-Osagean), the Antler Orogeny, which is in part represented by the thrusting and emplacement of the Roberts Mountain Allochthon, formed the Antler Highlands in western North America (Figure 2; Dickinson, 2006; Giles and Dickinson, 1995; Speed and Sleep, 1982). Within what is now southeastern Nevada, Late Devonian to Early Mississippian shales and carbonates (Figure 3), including the Pilot Shale, Joana Limestone, Limestone X, and Monte Cristo Group, were deposited in a migratory

backbulge-forebulge system of the Antler Foreland Basin (Dickinson, 2006; Goebel, 1991; Giles and Dickinson, 1995; Giles, 1996).

Near Alamo, Nevada in the Pahranagat Range, Reso (1963) described the Devonian Pilot Shale as black shale with limestone concretions. The Mississippian Joana Limestone and overlying Limestone X alternately have been assigned either to two separate units (Singler, 1987) or a single formation (Reso, 1963). This study uses the stratigraphic nomenclature of Singler (1987) (Figure 3). The Joana Limestone was described as a grainstone to packstone facies that was deposited during sea-level transgression, and Limestone X was interpreted as a deep-water (100-200 m water depth) deposit with interbeds of sediment that was transported from adjacent shallow-water platforms (Singler, 1987). Evidence for deep-water deposition was mainly from the conodonts that are reported to be deep-water forms (Singler, 1987). Two conodont zones were reported from Limestone X: *Siphonodella isosticha* of Late Kinderhookian age from the lower 64 meters of Limestone X, and *Gnathodus typicus* of Early Osagean age from the upper 102 meters. The lack of diagnostic conodonts from the middle 36 meters of Limestone X leaves the Kinderhookian–Osagean boundary undetermined in this section.

The Joana Limestone and Limestone X are stratigraphically correlated to the Monte Cristo Group in the Arrow Canyon Range of southeastern Nevada. The group includes, in ascending order, the Crystal Pass Formation, Dawn Limestone, Anchor Limestone and Bullion Limestone (Fig. 3; Pierce, 1969; Hansen and Carozzi, 1974; Pierce and Langenheim, 1974). Conodont forms *Polygnathus communis communis* and *Pseudopolygnathus dentilineatus* in the Dawn Limestone and the lower Anchor Limestone indicate their Kinderhookian–Osagean age (Pierce and Langenheim, 1974).

The Kinderhookian–Osagean boundary was placed at the first appearance of *Polygnathus communis carinus* in the Anchor Limestone. Overall, the Monte Cristo Group represents deposition in shallow, open-marine environments with intermittent quiet, deep-water channels (Hansen and Carozzi, 1974). The Dawn Limestone was interpreted as consisting of wackestone-to-packstone facies deposited during a transgression, and the Anchor and Bullion limestones are composed predominantly of crinoidal packstone-to-grainstone facies, and interpreted to have been deposited during a regression (Hansen and Carozzi, 1974).

CHAPTER 3

PREVIOUS WORK ON THE TOURNAISIAN CARBON ISOTOPE EXCURSION

The Tournaisian positive $\delta^{13}C_{carb}$ excursion has been reported from numerous Upper Devonian to Lower Carboniferous sections in North America, Europe, and Asia (Figure 4). The global correlation of this $\delta^{13}C_{carb}$ excursion is constrained by the presence of the *Siphondella isosticha* and *Gnathodus typicus* conodont zones of Tournaisian (International term) or Kinderhookian–Osagean (North American terms) age (Figure 3).

Budai et al. (1987) first reported $\delta^{13}C_{carb}$ values up to +7‰ within the *S. isosticha* conodont zone of the Madison Group in Wyoming and Utah of the western U.S. Bruckshen and Veizer (1997) documented this $\delta^{13}C_{carb}$ excursion with peak values of +6‰ from time-equivalent strata in the Dinant Basin of western Europe. Soon thereafter, Mii et al. (1999) documented δ13C and δ18O of nearly 600 brachiopod samples from the Central United States, including multiple sites in Texas, Oklahoma, Kansas, Illinois, Iowa, Missouri, and single sites in Nebraska and Canada. The results revealed a positive $\delta^{13}C$ excursion with maximal values >+6‰ of late Kinderhookian to early Osagean age. They also found a 3‰ to 5‰ increase in $\delta^{18}O$ across the $\delta^{13}C_{carb}$ excursion. Saltzman et al. (2000) and Saltzman (2002) reported the excursion with peak $\delta^{13}C_{carb}$ values up to +7.1‰ from the Pahranagat Range and Arrow Canyon Range in southern Nevada. In addition, similar $\delta^{13}C$ values and trend have been reported from the Samaria Mountain in southeast Idaho (Saltzman, 2002), East Tintic Range and the Uinta Mountains in Utah, and Beartooth Range and Salt River Range in Wyoming (Saltzman, 2003b).

A more comprehensive review of the Early Mississippian carbon and oxygen isotope record is provided by Buggisch et al. (2008). In numerous sites in North America and Europe, Early Mississippian $\delta^{13}C_{carb}$ records show two prominent positive $\delta^{13}C_{carb}$ excursion at the late Tournaisian (ca. 351 Ma) and late Serpukhovian (Ca. 322 Ma), respectively. Oxygen isotope values obtained from apatites (conodonts) show a positive shift of +2‰ across the Tournaisian positive $\delta^{13}C_{carb}$ excursion, which has an average amplitude of +6.5‰. They interpret the +2‰ shift in $\delta^{18}O$ to represent a seawater temperature decrease of 8-10°C across the Tournaisian $\delta^{13}C_{carb}$ excursion. However, the exact stratigraphic level of temperature decrease and its relationship with the $\delta^{13}C_{carb}$ excursion is still debatable because of the scatter of data points and translation of data from multiple sections into a composite curve. Buggisch et al. (2008) also conducted a limited number of organic carbon isotope analyses, but the organic carbon isotopes show much larger variations compared with the carbonate carbon isotopes. Thus high-resolution, integrated $\delta^{13}C_{carb}$, $\delta^{18}O$, and $\delta^{13}C_{org}$ analyses from representative sections are still needed to better understand the coupling of the carbon cycle and seawater temperature change.

CHAPTER 4

METHODS

A total of 237 limestone samples were collected from two stratigraphically correlated sections, among which 182 samples came from the section near Alamo in the southern Pahranagat Range and 55 came from Tungsten Gap in Arrow Canyon. In each section, samples cover the Tournaisian positive $\delta^{13}C_{carb}$ excursion, as guided by existing data in the literature (Saltzman et al., 2000; Saltzman, 2002, 2003a). In addition, brachiopod samples were collected wherever they were observed in the Alamo section.

All samples were microdrilled from clean, fresh surfaces in the finely-crystalline, darkest portions of the limestone samples to minimize influences from secondary recrystallization, tectonic fractures, and surficial organic matter contamination. Brachiopod samples were separated and microdrilled by Dr. Uwe Brand at Brock University following his methodology for brachiopod preparation. Brachiopod samples were analyzed for both $\delta^{13}C_{carb}$, and $\delta^{18}O$, but not $\delta^{13}C_{org}$ because the volume of individual samples recovered was too small for reproducible $\delta^{13}C_{org}$. Brachiopod trace element analysis was conducted by Dr. Brand at Brock University following his methodology.

Samples for each set of $\delta^{13}C_{carb}$, $\delta^{18}O$, and $\delta^{13}C_{org}$ analyses were extracted from the same sample powders. For carbonate carbon and oxygen isotope analysis, 50-200 µg of carbonate powder were reacted with orthophosphoric acid for 10 minutes at 70°C in a Kiel-Device automatically connected to a Finnigan dual-inlet Delta Plus, mass spectrometer. The results are reported in the standard δ-notation as per mil (‰) deviations from Vienna-Pee Dee belemnite (VPDB). Precision of analysis was

determined by multiple measurements of National Bureau of Standards (NBS)-19 and by an internal standard repeated every 8 samples. The precision is better than 0.05‰ for both $\delta^{13}C_{carb}$ and $\delta^{18}O$.

Samples for $\delta^{13}C_{org}$ analysis were prepared following an expanded version of the acid fumigation method presented by Harris et al. (2001) to ensure complete removal of all carbonate material within the samples. Prior to preparation, sample powders were dried in an oven at 105°C for 12 hours. After drying, 30-45 mg sample powders were weighed and placed in open-ended Costech (9 by 5 mm) silver capsules. The silver capsules were then placed in a quartz sample tray. Deionized (DI) water was added to each capsule to moisten the sample powders to approximately the field capacity (Harris et al., 2001). The sample tray and a 150 milliliter beaker filled with 100 milliliters of concentrated 12 M HCL were placed in a 5 liter vacuum desiccator for acid fumigation and carbonate removal for 12 hours (Hedges and Stern, 1984; Harris et al., 2001). The samples were then removed from the desiccator and placed directly into an oven at 70°C to dry for 4 hours. One drop of 1 M HCL was added into each silver capsule to ensure complete carbonate removal. If samples had not achieved complete carbonate removal, several drops of 1 M HCL were added to each capsule as needed to react with remaining carbonate and returned to the 70°C oven for another 4 hours. Samples were tested again until all carbonate was removed. Once complete carbonate removal was achieved, samples were placed in 20 ML plastic hexagonal weigh dishes filled with DI water to wash the remaining acid in the silver capsules and sample residues. Before transferring samples from the quartz tray to the weigh dishes, the silver capsules were filled with DI water to avoid tilting and loss of sample residue during the transfer process. The samples

stayed in the DI water for 8-12 hours and then were placed back into the 70°C oven to dry for 4 hours. This washing and drying process was repeated between 3-6 times until pH tests of the water gave neutral values (>6).

The samples, free of carbonate and acid, were then placed back into the 70°C oven for 12 hours to ensure complete removal of all moisture from the capsules and sample residues. The silver capsules were then wrapped up into tin capsules and stored in the 70°C oven until analysis. The carbon and nitrogen contents along with organic carbon isotope analysis were analyzed using an elemental analyzer (EA) coupled with a conflow interface that automatically transfers carbon dioxide gas into a Finnigan Delta Plus mass spectrometer. Isotopic values are reported in per mil (‰) vs. VPDB. USGS-24 (graphite), IAEA-600 (caffeine), and Costech Analytical Technologies acetanilide standards were used to monitor internal and external uncertainties that were better than 0.2‰ for $\delta^{13}C_{org}$ and 0.1% for total organic carbon content (TOC). To ensure reproducibility of both organic-rich and organic-poor samples, duplicates were placed in every 5 samples, and the resultant reproducibility in $\delta^{13}C_{org}$, and TOC was better than 0.15‰ and 0.2%, respectively. All the carbonate carbon, oxygen, and organic carbon isotope analyses were conducted in the Las Vegas Isotope Science (LVIS) lab at the Department of Geoscience, University of Nevada, Las Vegas.

CHAPTER 5

RESULTS

5.1 Stratigraphy of Measured Sections

5.1.1 The Alamo Section in the Pahranagat Range

The Upper Devonian to Lower Mississippian strata in the Pahranagat Range near Alamo include the uppermost Pilot Shale, Joana Limestone, and Members A-D of Limestone X (Singler, 1987). Stratigraphic analyses and sample collection are correlated with the conodont biozones (Singler, 1987), which are the primary geochronological constraints in this section (Figures 5 and 6; Appendix 3).

The first 9 meters of this section are within the Devonian Pilot Shale, and are composed of dark-gray to black shale with lime mudstone and grainstone interbeds. Brachiopods are sparse in the black shale and lime mudstone. Toward the top of the Pilot Shale the lithology grades into gray to dark-gray, thin-bedded (1-5 cm thick) wackestone and grainstone with chert nodules, brachiopods, and crinoids. The 25-m-thick Joana Limestone marks the beginning of Mississippian age strata, and is mainly composed of gray to dark-gray grainstone with crinoids, brachiopods, rugose corals, and sparse chert nodules. Interbedded within the grainstone beds are dark gray wackestone to packstone beds with crinoids, brachiopods, and chert nodules.

Overlying the Joana Limestone is Limestone X, which was divided into four members (Members A-D) by Singler (1987). Member A is about 70 meters thick, and entirely within the *S. isosticha* conodont zone of Kinderhookian Stage. It is composed predominantly of gray to dark-gray, interbedded grainstone, packstone and wackestone

with brachiopods, crinoids, corals (both rugose and tabulate corals), and rare chert nodules. The thickness of the wackestone, packstone, and grainstone layers varies from a few centimeters to decimeters, forming a cyclic pattern. The middle to upper 25-30 meters (61-93m) of Member A, however, is wackestone-to-packstone dominated, fractured, and virtually devoid of fossils. Member B is 60 meters thick and is within the *S. isosticha* conodont biozone. Its top appears to be coincident with the end of the Kinderhookian Stage. The lower 30 meters of Member B (110-140m) are mainly dark to dark-gray, bioturbated wackestone interbedded with thin (1-5 cm thick), laterally discontinuous grainstone. Shale partings (< 2 cm thick) are common at the wackestone-grainstone contact and within the grainstone beds. Visible fossils include crinoids, brachiopods, corals (both tabulate and rugose) and trace fossil *Zoophycos*. Strata from 140-147m is composed of alternating, dark-gray, medium-bedded (10-25 cm thick) grainstone and wackestone with rare chert nodules, crinoids, brachiopods, and rugose corals. The overlying 5 meters (147-152m) is dark-gray packstone to wackestone that grade into dark-gray, fossil-rich grainstone. The uppermost 12 meters of Member B (152-164m) is composed of medium-bedded (10-20 cm thick), dark-gray wackestone with rare small chert nodules, with abundant fossils including brachiopods, bryozoans, crinoids, corals, and weak to moderate bioturbation.

Member C is 58 meters thick and locally marks the beginning of the Osagean Stage and the *G. typicus* conodont zone. It begins with 5 meters (167-172m) of dark-gray to-gray wackestone with shaly partings and sparse chert nodules. Abundant visible fossils in this interval include brachiopods, crinoids, and rugose and tabulate corals that form bioherms approximately 1 meter thick. The overlying 5 meters of Member C (172-177m)

are composed of alternating dark gray, 10 to 30-cm-thick wackestone and 1 to 5-cm-thick floatstone. Both facies contain crinoids, brachiopods, solitary rugose corals, and small bioherms of tabulate colonial coral. The overlying 20 meters of Member C (177-199m) are comprised of dark-gray to gray, medium to thick-bedded (15-40 cm) wackestone with increasingly common chert nodules. Fossils observed within this interval include brachiopods, crinoids, bryozoans, and tabulate and rugose corals. The next 6 meters (199-205m) consist of dark to gray, thin-to-medium-bedded (10-30 cm) wackestone with 3 to 5-cm-thick grainstone interbeds and less than 2 cm-thick shaly partings. Member C continues with 18 meters (205-222m) of dark-gray, thin-to-medium-bedded (10-30 cm thick) wackestone with common thin (1-2 cm) shaly layers, grainstone, and packstone. The top 4 meters (222-226m) of Member C are composed of dark-gray wackestone with rare shaly partings, and rare to common brachiopods, crinoids, gastropods, and solitary rugose corals.

Member D of Limestone X is 56 meters thick and is within the *G. typicus* conodont zone of the Osagean stage. The basal 8 meters (226-234m) is medium-gray-to-dark-gray wackestone with thin (1-5 cm thick), laterally discontinuous, lime-mudstone to grainstone beds. Brachiopods, gastropods, and corals are common, along with chert nodules and weak to moderate bioturbation. The overlying 38 meters (234-272m) are comprised of dark gray, thin-to-medium-bedded wackestone with interbedded, 1 to 10 cm thick dark-gray grainstone. Brachiopods, corals, crinoids, bioturbation, and chert nodules were common throughout this interval. Chert abundance increases from rare nodules in the lowest 20 meters to more abundant and large (>2 cm in diameter) chert nodules in the upper 18 meters of this interval. This interval is overlain by 2 m thick (272-274m), dark-

gray wackestone with thin (<5 cm), lenticular grainstone layers that contain abundant solitary rugose corals, brachiopods, crinoids, and the trace fossil *Zoophycos*. The final 8 meters (274-282m) of Member D are composed of dark-gray grainstone with rare to common chert nodules, brachiopods, and crinoids, rugose and tabulate corals.

5.1.2 The Tungsten Gap Section in Arrow Canyon

The Tungsten Gap section in Arrow Canyon includes Late Devonian to Early Mississippian strata (Figure 7; Appendix 3) that have been biostratigraphically correlated with other sections in the U.S. and globally (Langenheim, 1969; Hansen and Carozzi, 1974). The base of the Tungsten Gap section is within the Devonian Crystal Pass Limestone. The lowest 12 meters (0-12m) of this unit are composed of medium- to thick-bedded (20-40 cm thick), light-gray to gray packstone devoid of visible fossils. The overlying 5 meters (12-17m) consist of thinly laminated (1-3 cm), dark-gray wackestone with rare fossil fragments. The overlying 7 meters (17-24m) is light-gray to buff-colored, thick-bedded (30-60 cm) lime-mudstone with rare brachiopod fragments and chert nodules.

Overlying the Crystal Pass Limestone is the 63-meter-thick Dawn Limestone of Early Mississippian age. The lowest 22 meters (24-46m) of the Dawn Limestone are composed of alternating layers of massively-bedded packstone and wackestone with rare tabulate coral bioherms, brachiopods and unidentified shell fragments. The overlying 5-m-thick (46-51m), cross-bedded grainstone layer contains small tabulate coral bioherms. This unit is overlain by 5 meters (51-56m) of alternating, gray-to-dark-gray grainstone and packstone with no visible fossils. The overlying 7 meters (56-63m) are medium-bedded (10-20 cm), gray-to-dark-gray grainstone with small tabulate coral bioherms overlain by

3 meters (63-66) of thin-bedded (~10 cm), dark-gray wackestone with thin (1-3 cm thick) lime-mudstone layers. The uppermost 21 meters (66-87) of the Dawn Limestone are composed of alternating, gray-to-dark-gray, thick-bedded (15-40 cm) grainstone and medium-to-thick-bedded (15-40 cm) packstone with rare crinoids, brachiopods, and chert nodules. Overall, the Dawn Limestone at Tungsten Gap has rare visible fossils and very rare chert nodules that distinguish it from the overlying Anchor Limestone.

Only the lower 27 meters of the Anchor Limestone were measured in this section. The lower 11 meters (87-98m) are gray wackestone with interbedded cherts that are 10-20 cm thick. The overlying 10 meters (98-108m) is light-gray to gray, thin-to-medium-bedded (10-25 cm) wackestone with 10 to 20cm thick interbedded chert, and rare to common crinoids and corals. The uppermost unit measured is the overlying 6 meters (108-114m) of gray, medium to thick-bedded (20-40 cm) grainstone with an increase in abundance of solitary rugose and tabulate corals, brachiopods, crinoids, and chert nodules from rare to common.

5.2 Isotope Results

5.2.1 Isotope results from the Alamo Section

The $\delta^{13}C_{carb}$ values from the upper part of the Devonian Pilot Shale are between -1‰ and 0‰ and increase to between +2‰ to +3‰ in the Mississippian Joana Limestone (Figure 5, Appendix 1). Within Member A of Limestone X, $\delta^{13}C_{carb}$ values increase from near +2‰ at the base to around +6‰ at the top of Member A. Peak $\delta^{13}C_{carb}$ values of +7.1‰ occur at the base of Member B and remain between +6‰ to +7‰ for the next 12 meters. The $\delta^{13}C_{carb}$ values show a small negative shift from +7‰ to +4‰ in the middle of Member B and then increase to more positive values from +4‰ to +7.4‰ near the top

of Member B. For the majority of Member C, $\delta^{13}C_{carb}$ values remain stable between +6‰ and +7‰. A decrease in $\delta^{13}C_{carb}$ from +7‰ to +1.8‰ occurs in the last 46 meters of the section that covers the uppermost part of Member C and Member D.

The $\delta^{18}O$ values in this section increase from -6.7‰ in the Pilot Shale to -4.1‰ at the top of the Joana Limestone. A large negative shift from -4.4‰ to a minimum down to -21‰ occurs in the lower part of Member A, which is followed by a positive shift from -21‰ to -4‰ near the top of Member A (Figures 5 and 6). The majority of $\delta^{18}O$ values from the top of Member A to Member D are within -4‰ to -3‰, except for a few data points in the upper part of Member B that go down to -5‰ to -6.5‰, and another few in the lower Member B and upper Member C that reach higher values of about -2‰.

The $\delta^{13}C_{org}$ values increase from -29.5‰ in the Pilot Shale to -23‰ in the lower part of the Joana Limestone. From the upper Joana Limestone to the lower 50 meters of Member A, $\delta^{13}C_{org}$ values are fairly stable between -26‰ and -24‰. An increase in $\delta^{13}C_{org}$ from -27‰ to -23‰ is observed in the upper part of Member A through lower part of Member B. A negative shift in $\delta^{13}C_{org}$ from -23‰ to -27‰ occurs at the middle part of Member B, coincident with the negative shift in $\delta^{13}C_{carb}$ from +7‰ to +4‰ (Figure 5). From the uppermost Member B to Member C, most of the $\delta^{13}C_{org}$ values fall in the range of -24‰ to -25‰. A negative shift in $\delta^{13}C_{org}$ from -24‰ to -28‰ occurs within Member D, similar to the trend recorded in $\delta^{13}C_{carb}$. It should be noted that a few $\delta^{13}C_{org}$ data points, including values of -20.4‰ at 47.9 m (lower Member A), -21.8‰ at 183.8 m (lower member C), -22.4‰ and -22.6‰ at 240.9 m and 246 m (lower Member D), and -21.6‰ at 282 m (Member D), are questionable because of their departure from adjacent samples and inconsistence with corresponding $\delta^{13}C_{carb}$ values. This

inconsistence is likely due to incomplete removal of carbonates during sample preparation. Thus, these points need to be reanalyzed in the future, but are not used in the trend analysis of this study.

The $\Delta\delta^{13}C$ ($\Delta\delta^{13}C=\delta^{13}C_{carb}-\delta^{13}C_{org}$) values from the Pilot Shale, Joana Limestone, and Member A are quite variable between 29‰ and 25‰, but overall they show an increase from an average of 28‰ in the Pilot Shale and Joana Limestone to an average of 31‰ in uppermost Member A. Most of the $\Delta\delta^{13}C$ values of Member B through lower Member D are stable, with an average close to 31‰. A minor decrease from 31‰ to 30‰ is present in upper Member D. Again, the few data points with uncertain $\delta^{13}C_{org}$ values show an obvious departure in $\Delta\delta^{13}C$ from the average values of adjacent samples (Figure 5).

5.2.2 Carbonate Carbon and Oxygen Isotopes from Brachiopods

Brachiopod samples were chosen from 13 horizons across the $\delta^{13}C$ excursion in the Alamo section to test if they preserve better oxygen isotope values than their hosting micritic matrix (Figure 6, Appendix 2). Brachiopods from two stratigraphic horizons in the Pilot Shale record higher $\delta^{13}C_{carb}$ and lower $\delta^{18}O$ values than their hosting matrix. Within the Joana Limestone and lower part of Member A, brachiopod $\delta^{13}C_{carb}$ and $\delta^{18}O$ values are identical to those of their hosting matrix. Brachiopods from the two stratigraphic horizons across the maximum of the $\delta^{13}C_{carb}$ excursion produce $\delta^{13}C_{carb}$ and $\delta^{18}O$ values that compare favorably to those of the matrix, with the exception of two samples that show $\delta^{13}C_{carb}$ values 1-2‰ lower than those of the matrix. Brachiopods from the other six stratigraphic horizons of Member C and D have $\delta^{18}O$ values similar to those of their corresponding host matrix, but they have relatively lower $\delta^{13}C_{carb}$ values. Overall, for the entire section, brachiopod samples have $\delta^{13}C_{carb}$ and $\delta^{18}O$ values in the range that

encompasses $\delta^{13}C_{carb}$ and $\delta^{18}O$ values of their hosting matrix, except for the cases of the Pilot Shale, from which brachiopods have somewhat higher $\delta^{13}C_{carb}$ and lower $\delta^{18}O$ values compared to their host micritic matrix.

5.2.3 Isotope Results from the Tungsten Gap Section

In the Tungsten Gap section, $\delta^{13}C_{carb}$ values from the uppermost Crystal Pass Limestone are between 0‰ and -1.3‰ (Figure 7, Appendix 1). The first 10 meters of the Dawn Limestone has $\delta^{13}C_{carb}$ values near +1.0‰, followed by an increase to peak values up to +4.7‰ within a 15-m-thick interval. The $\delta^{13}C_{carb}$ values from the middle part of the Dawn Limestone (44 to 78 m of the section) show frequent changes between +1.1‰ and 4.3‰. The uppermost part of the Dawn Limestone (78 to 86 m) and the lower Anchor Limestone (86 to 108 m) show a negative anomaly from +3.2‰ to +1.3‰ and then back to +3.0‰. The last 6 meters of the Anchor Limestone measured show another negative shift from +3.0‰ to +1.7‰.

Oxygen isotopes from the Crystal Pass Limestone are between -7‰ and -8.2‰. Samples from the Dawn Limestone have quite variable $\delta^{18}O$ values, mostly between -8‰ and -4‰, with two minimum values down to -10.6‰ at 50 m and -8.8‰ at 82 m (Figure 7). A positive peak with $\delta^{18}O$ value of -2.9‰ is present in the lower Anchor Limestone (98 m), followed by a negative shift down to values between -6.5‰ and -4.5‰ for the rest of the section.

The $\delta^{13}C_{org}$ values show a positive shift, from -31‰ in the Crystal Pass Limestone to -21.5‰ in the lower Dawn Limestone (0-32 m). The middle part of the Dawn Limestone, from 32m to 62 m, has stable $\delta^{13}C_{org}$ values around -25‰. A minor negative excursion with minimum $\delta^{13}C_{org}$ values down to -26.8‰ occurs in the upper part of the Dawn

Limestone and lower Anchor Limestone (62-100 m). The uppermost 14 meters of the section has $\delta^{13}C_{org}$ values back to between -24‰ to -25‰.

From the Crystal Pass Limestone to the lower Dawn Limestone (0-44 m), the $\Delta\delta^{13}C$ values show a negative excursion that starts with values around 30‰, down to a nadir of 23.6‰, and back to 30.2‰ (Figure 7). In the middle part of the Dawn Limestone, from 44 m to 74 m, the $\Delta\delta^{13}C$ values are variable between 25‰ and 29.4‰, but they do not reveal a clear trend. From the upper Dawn Limestone through the Anchor Limestone (74-114 m), $\Delta\delta^{13}C$ values decrease from 29.4‰ to 26.7‰.

CHAPTER 6

DISCUSSION

The original hypothesis of this study was that $\delta^{13}C_{carb}$ and $\delta^{13}C_{org}$ values, as recorded in the Alamo and Tungsten Gap sections, would covary if the positive $\delta^{13}C_{carb}$ excursion was formed through increased organic burial. At the same time, one would expect to see a global cooling because increased organic burial would lower atmospheric CO_2, which should be recorded as a positive shift in $\delta^{18}O$ values across the $\delta^{13}C_{carb}$ excursion. In addition, lower atmospheric CO_2 may lead to a decrease in photosynthetic carbon isotope fractionation (Hayes et al., 1999; Kump and Arthur, 1999), which should be reflected by decreasing $\Delta\delta^{13}C$ values across the $\delta^{13}C_{carb}$ excursion.

Overall, this study demonstrates positive shifts in both $\delta^{13}C_{carb}$ and $\delta^{13}C_{org}$, which implies that carbon isotopes of the surface ocean DIC (recorded by $\delta^{13}C_{carb}$) exercised a first-order control on the carbon isotopes of organic matter ($\delta^{13}C_{org}$). The $\delta^{13}C_{carb}$ profile from the Alamo section mirrors that of Saltzman (2002). Globally, sections from the United States, Canada, Russia, and Belgium record a fairly consistent $\delta^{13}C_{carb}$ excursion with a peak of +5‰ to +7.1‰ (Bruckshen and Veizer, 1997; Mii et al., 1999; Saltzman et al., 2000; Saltzman, 2002; Saltzman, 2003; Saltzman et al., 2004; Buggisch et al., 2008). Thus the results from this study confirm that the Tournaisian (Early Mississippian) $\delta^{13}C_{carb}$ excursion records a major perturbation in the global carbon cycle.

However, the data from the two sections also have variations that are not consistent with the hypothesized predictions. First, the magnitude of the $\delta^{13}C_{org}$ excursion is smaller than that of the $\delta^{13}C_{carb}$ excursion, and there are more $\delta^{13}C_{org}$ variations than $\delta^{13}C_{carb}$ in some intervals. Second, there are significant differences in $\delta^{13}C$ and $\delta^{18}O$ between the

two measured sections. Third, $\delta^{18}O$ values increase before the $\delta^{13}C_{carb}$ and $\delta^{13}C_{org}$ peaks, but do not have significant changes at and after the $\delta^{13}C$ peaks. The origin of these discrepancies is discussed below.

6.1 Possible Origins of Larger Variations in $\delta^{13}C_{org}$

Carbon isotopes of sedimentary carbonates record $\delta^{13}C$ of oceanic DIC, which is presumably homogeneous in open-marine seawater, while $\delta^{13}C$ of organic matter is controlled by various environmental factors (Figure 8), such as differential fractionation of organisms (ecosystems) during carbon fixation, CO_2 concentration in seawater, and growth rate (production rate). In general, higher $CO_{2(aq)}$, smaller organisms, and lower growth rate lead to higher photosynthetic carbon isotope fractionation and lower $\delta^{13}C_{org}$ values (e.g., Hayes et al., 1999; Raven et al., 2002). Thus, even if the total organic carbon is from photosynthetic carbon fixation, the environmental variance in $\delta^{13}C_{org}$ is twice that of $\delta^{13}C_{carb}$ (Derry et al., 2010). Furthermore, in some cases the total organic matter in sediments is not merely from primary production; contributions may come from secondary production, including detrital fossil organic carbon and dissolved organic carbon (DOC) in seawater (Figure 8), that is isotopically different from primary production. Secondary producers including heterotrophic, chemoautotrophic, and methanotrophic organisms that are common in anoxic environments may change the isotopic composition of organic matter. While heterotrophic organisms tend to produce organic carbon that has higher $\delta^{13}C_{org}$ values than co-existing photosynthetic organisms (e.g., Hayes et al., 1989), chemoautotrophic and methanotrophic organisms produce organic carbon that has much lower $\delta^{13}C_{org}$ values because they use ^{13}C-depleted CO_2 (from organic matter decay) or methane as the carbon source during carbon fixation (e.g.,

Conway et al., 1994; Summons et al., 1994). Detrital fossil organic carbon contribution to total organic matter is more common in proximal areas of continental shelves or in areas close to riverine inputs. Dissolved organic carbon (DOC) in seawater, which may have been important in certain times of the geological history (e.g., Neoproterozoic; Rothman et al., 2003), constitutes only a small portion of the carbon reservoir in the modern ocean and perhaps in most of the Phanerozoic oceans because DOC has a low survival rate in oxygenated seawater at geological time scales.

Diagenesis, mainly methanogenesis and metamorphism, would release isotopically depleted CH_4/CO_2 from sediments, leaving ^{13}C-enriched organic matter in residual sediments and sedimentary rocks. These processes would lead to higher $\delta^{13}C_{org}$ values in bulk organic matter. However, Hayes et al. (1983) showed that diagenesis and metamorphism typically shift $\delta^{13}C_{org}$ towards higher values on the order of 2−3‰ for rocks metamorphically lower than greenschist facies. Hydrocarbon contamination is commonly controlled by fluid pathways and should be lithologically distinct. No such contamination was observed in either section of this study.

Data from the Alamo section show overall coupled $\delta^{13}C_{carb}$ and $\delta^{13}C_{org}$, implying that the organic matter was mainly from primary production. In this case, $\delta^{13}C_{org}$ was mainly controlled by $\delta^{13}C$ of seawater DIC (DIC = $CO_{2(aq)} + HCO_3^- + CO_3^{2-}$), from which photosynthetic organisms used $CO_{2(aq)}$ as the carbon source during carbon fixation. Second-order variations in $\delta^{13}C_{org}$ may have originated from environmental changes through time, in which organisms and/or their production rates changed over time scales shorter than that of DIC.

The temporal variations in $\delta^{13}C_{org}$ (Figure 7) and lack of $\delta^{13}C_{carb}$–$\delta^{13}C_{org}$ covariation (Figure 9B) from the Tungsten Gap section, however, cannot be explained with confidence. In this section, the $\delta^{13}C_{carb}$ values also show large temporal variations suggestive of diagenetic modification (see next section). Therefore the lack of covariation of $\delta^{13}C_{carb}$ and $\delta^{13}C_{org}$ may be due to diagenetic modification of $\delta^{13}C_{carb}$. Temporal variations over time scales shorter than $\delta^{13}C_{carb}$ may be influenced by the detrital organic carbon contribution or meteoric water inputs that changed the isotope values of local seawater DIC, assuming that the organic matter was from primary production.

6.2 Isotope Variations between Alamo and Tungsten Gap Sections

The absolute $\delta^{13}C_{carb}$–$\delta^{13}C_{org}$ values and trends differ between the two measured sections. These differences may be caused by local environmental changes or diagenesis. Diagenesis, including meteoric and burial, involves isotopically distinct fluids that commonly have more negative $\delta^{13}C_{carb}$ and $\delta^{18}O$ values than marine carbonates. As a result, diagenetic modification commonly shifts both $\delta^{13}C_{carb}$ and $\delta^{18}O$ of carbonates towards more negative values. However, diagenetic alteration commonly changes $\delta^{18}O$ more significantly than $\delta^{13}C_{carb}$ because meteoric or formation fluids contain much less carbon than oxygen (which is from water) (Banner and Hanson, 1990). Therefore, one of the criteria used to evaluate the degree of diagenetic alteration is to look at the $\delta^{13}C_{carb}$–$\delta^{18}O$ covariation: covariation indicates that diagenesis has altered both $\delta^{13}C_{carb}$ and $\delta^{18}O$. If there is no covariation, $\delta^{18}O$ values may have been altered, while $\delta^{13}C_{carb}$ are unaltered (Banner and Hanson, 1990; Kaufman and Knoll, 1995). The $\delta^{13}C_{carb}$–$\delta^{18}O$ cross-plot from the Alamo section (Figure 10A) shows a moderate covariation with $R^2 = 0.43$ (Figure 10A), while the $\delta^{13}C_{carb}$–$\delta^{18}O$ cross-plot from the Tungsten Gap section (Figure

10B) shows no covariation. Does that mean that the $\delta^{13}C$ and $\delta^{18}O$ values from the Alamo section are more severely altered by diagenesis?

Evidence has shown that using $\delta^{13}C_{carb}$–$\delta^{18}O$ covariation to evaluate the degree of diagenetic alteration may be invalid in many cases when diagenesis has completely reset the $\delta^{18}O$ values of carbonates (e.g., Allan and Matthews, 1982; Kanuth and Kennedy, 2009). A more reliable criterion is the covariation of $\delta^{13}C_{carb}$ and $\delta^{13}C_{org}$. Because no known diagenetic process can shift both $\delta^{13}C_{carb}$ and $\delta^{13}C_{org}$ toward the same direction at a similar magnitude, covarying $\delta^{13}C_{carb}$ and $\delta^{13}C_{org}$ indicates no significant diagenetic alteration (Knoll et al., 1986). Using this criterion, the isotope data obtained from the Alamo section are much more reliable than those from the Tungsten Gap section. The Alamo section data are consistent with the global correlation that shows a $\delta^{13}C_{carb}$ excursion with comparable magnitude (Buggisch et al., 2008). Therefore, one of the possibilities for the large $\delta^{13}C_{carb}$ variation, lower $\delta^{18}O$ values, and lack of $\delta^{13}C_{carb}$ and $\delta^{13}C_{org}$ covariation in the Tungsten Gap section is significant diagenetic alteration.

Another possibility for the isotope differences in the Tungsten Gap section is an environmental control that may have influenced the $\delta^{13}C$ of local seawater DIC. Paleogeographically, the Tungsten Gap section was closer (proximal) to the shoreline of the carbonate platform (Figure 2). Meteoric water input from land may have changed the carbon and oxygen isotopes of local seawater, leading to changes in $\delta^{13}C_{carb}$ and $\delta^{18}O$ values of carbonates. As mentioned in the previous section, this process may have also caused changes in $\delta^{13}C$ of organic matter. If this were the case, more significant influences from meteoric water would be expected in sections toward more proximal shelf regions to the east (e.g., sections in western Utah), which remains to be tested.

Detrital organic carbon input could be another possible cause of variable $\delta^{13}C_{org}$ values in the Tungsten Gap section. However, paleogeographical reconstruction indicates that the Tungsten Gap section was located up to 200 miles from the shoreline (Figure 2). It is difficult, if possible, for detrital organic carbon to bypass the 200-mile wide carbonate platform to exert significant influence on the $\delta^{13}C_{org}$ values in the Tungsten Gap section.

Considering that $\delta^{13}C_{carb}$ and $\delta^{18}O$ values from the Tungsten Gap section may have been significantly altered by diagenesis, and the $\delta^{13}C_{org}$ values may have been influenced by local environmental factors, the Alamo section is better suited to record temperature changes across the $\delta^{13}C$ excursion.

6.3 Seawater Temperature Changes across the $\delta^{13}C$ Excursion

If increasing organic carbon burial was the cause of the $\delta^{13}C_{carb}$ excursion, then a simple mass balance calculation indicates that a +4‰ to +5‰ shift in $\delta^{13}C_{carb}$ requires a burial of 1.5×10^{20} g of carbon (Kump and Arthur, 1999; Saltzman et al., 2000). The overall covariance of $\delta^{13}C_{carb}$ and $\delta^{13}C_{org}$ from the Alamo section (Figure 5) indicate that the organic carbon was derived from primary production. Because primary (photosynthetic) producers uses $CO_{2(aq)}$ in seawater (which is in equilibrium with atmospheric CO_2) as the carbon source, the large amount of organic carbon burial would significantly lower the atmospheric CO_2 level. A global cooling event, which should be recorded by sea-level fall and ice sheet advance, is thus expected under this scenario. A comprehensive review by Buggisch et al. (2008) on the oxygen isotope record indicates that there was indeed global cooling following the Early Mississippian $\delta^{13}C_{carb}$ excursion. However, the timing of the cooling event was apparently variable across the globe and physical evidence of glaciation across the $\delta^{13}C_{carb}$ excursion has not yet been discovered.

Caputo (1985) documented Late Devonian (Famennian) glacial deposits in Brazil. He postulated that the glaciation began in the Late Devonian in central South America and continued through the entire Carboniferous to early Late Permian, with the ice centers migrating across South America and Africa toward Antarctica. Buggisch et al. (2008) pointed out that the first glacial deposits are recorded in the Amazon Basin in Brazil, Bolivia, and Peru at the Devonian-Carboniferous transition, based on the work of Caputo (1985) and Streel et al. (2000). However, Buggisch et al. (2008) noted that no glacial deposits are known from the time interval of the positive $\delta^{13}C_{carb}$ excursion. Garzanti and Sciunnach (1997) presented data supporting the occurrence of a minimum of four phases of glacial erosion and sedimentation in Gondwana by the mid-Mississippian. They further pointed out that glacial events may have occurred 30 m.y. earlier than the recorded, large-scale, late Carboniferous to early Permian glaciations. González-Bonorino (1990) examined the evidence for middle Carboniferous glaciation in Argentina, and he speculated that ice centers developed on the Patagonia highlands, possibly beginning in the Early Carboniferous.

The data from the Alamo section indicate that there is a 3‰ increase in $\delta^{18}O$, from -6‰ in the Devonian Pilot Shale to -3‰ higher in the section. Brachiopods from the Alamo section that were determined by trace element geochemistry to be unaltered (Figure 11; Brand, 2004) produce the same $\delta^{18}O$ trend. If the increase in $\delta^{18}O$ records seawater temperature change, a 12-15°C cooling (4.1-4.5°C drop with each 1‰ increase in $\delta^{18}O$; Hoefs, 2009) may have happened during the Early Tournaisian (before the end of Member A; see Figure 6). A very strong negative shift in $\delta^{18}O$, down to -21‰, occurs before the $\delta^{13}C_{carb}$ peak. Negative $\delta^{18}O$ values as low as -21‰ are most likely glacially

related (Ruddiman, 2001), but the spatial distribution and global representativeness requires further investigation. It may record the advance of ice sheets to the low-latitude ocean (e.g., Soreghan et al., 2008), or it could be influenced by Alpine-type ice from the Antler highlands. Burial diagenesis can be another process that could lower $\delta^{18}O$ values down to -21‰, but it is unlikely to be the cause of the large negative $\delta^{18}O$ shift because diagenesis should have reset the $\delta^{18}O$ of the entire Alamo section rather than a negative $\delta^{18}O$ excursion in the middle of the section. The potential global cooling event recorded by the oxygen isotopes in the Alamo section predates the peak of $\delta^{13}C_{carb}$ excursion, but its global synchrony needs to be confirmed in other successions around the globe.

CHAPTER 7

CONCLUSION

Carbonate and organic carbon isotope analyses in Alamo and Tungsten Gap sections confirm that the previously recognized Tournaisian (Early Mississippian) positive $\delta^{13}C_{carb}$ excursion records a major perturbation in the global carbon cycle. Coupled $\delta^{13}C_{carb}$ and $\delta^{13}C_{org}$ values in the Alamo section supports the interpretation that enhanced organic carbon burial was the driver of this large positive carbon isotope excursion. The variability in both $\delta^{13}C_{carb}$ and $\delta^{13}C_{org}$ in the Tungsten Gap section implies significant diagenetic overprint or local environmental influences on carbon isotope values. Oxygen isotope values of brachiopods and limestone matrix from the Alamo section record a 12-15°C decrease in temperature that predates the $\delta^{13}C_{carb}$ maximum. A strong negative shift in $\delta^{18}O$ down to -21‰ prior to the $\delta^{13}C$ peak suggests the advance of ice sheets to the low latitude ocean or local ice sheet expansion in the Antler highlands. Carbonate and organic carbon isotope fractionation, approximated by $\Delta\delta^{13}C$, increased prior to the $\delta^{13}C_{carb}$ peak and remained fairly static for the remainder of the measured and sampled Alamo section. The $\Delta\delta^{13}C$ change is consistent with the temperature changes, which suggests that the coldest climate occurred before the $\delta^{13}C$ peak, and remained static for the remainder of the excursion interval.

The new data from this study illuminate unresolved questions that need to be addressed. One such problem is the cause of the significant isotopic differences between the Alamo and Tungsten Gap sections. The more scattered and lower values in $\delta^{13}C_{carb}$, $\delta^{13}C_{org}$, and $\delta^{18}O$ from the Tungsten Gap section suggest a significant influence from meteoric diagenetic alteration. To test this interpretation, increased sample resolution is

required from the Tungsten Gap section, along with high resolution sampling of other sections further eastward in more proximal environments of the carbonate platform.

FIGURES

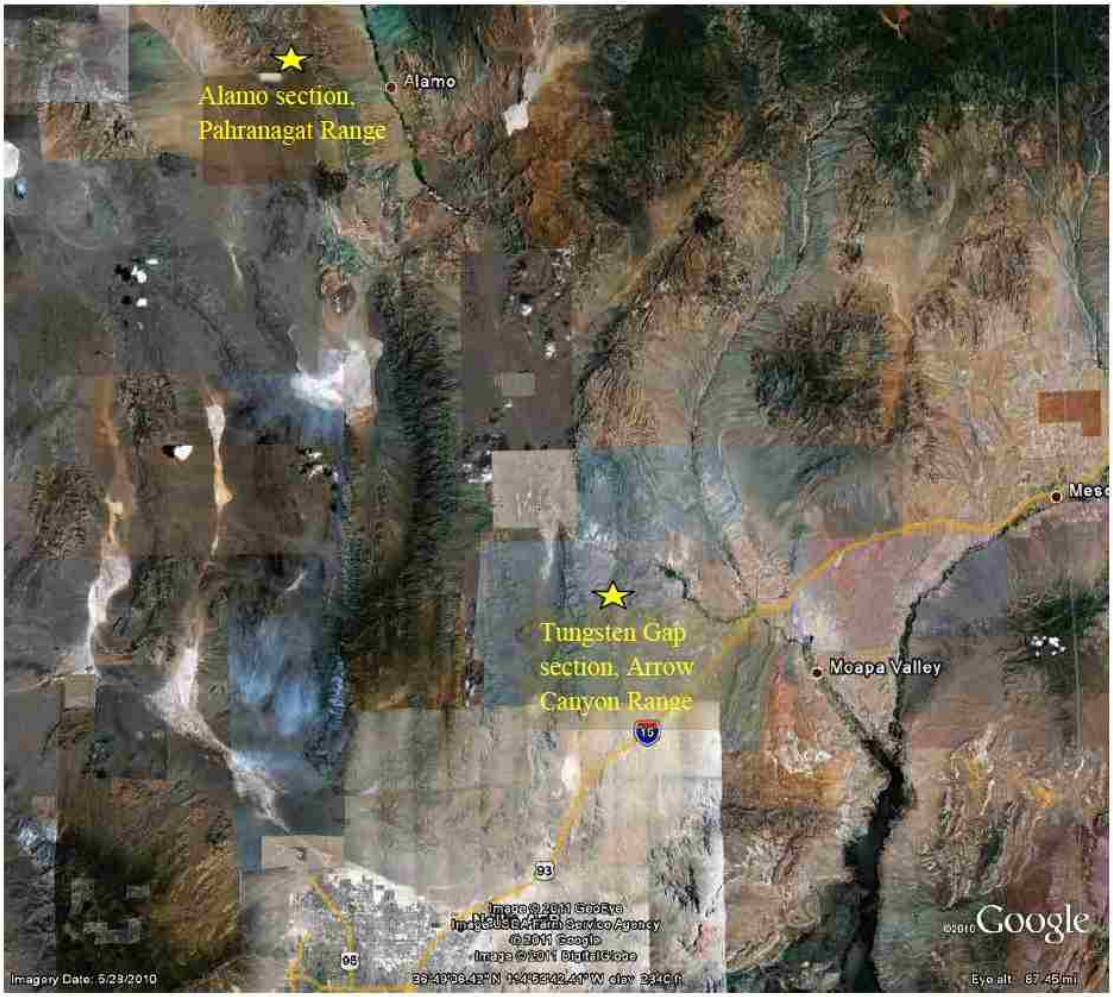

Figure 1. Location of the two measured sections, the Alamo section in the Pahranagat Range and the Tungsten Gap section in Arrow Canyon.

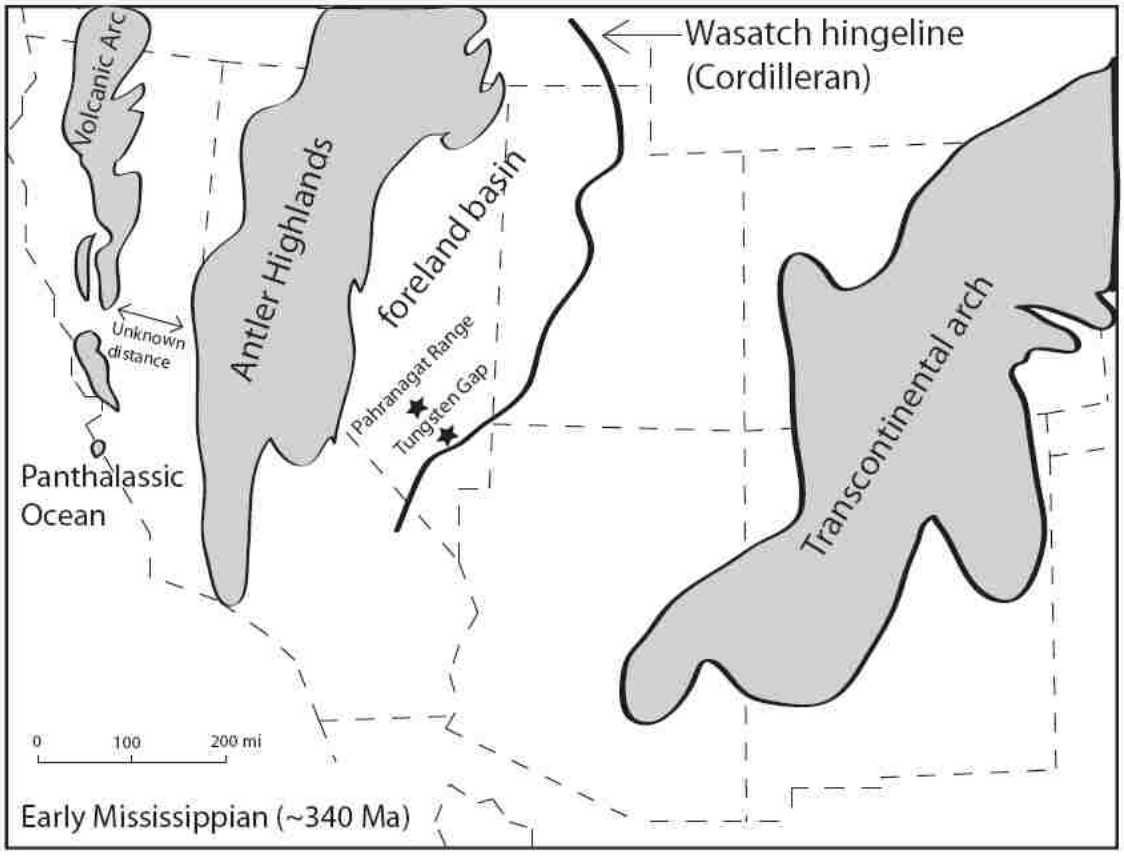

Figure 2. Non-palinspastic paleogeographic reconstruction of the western United States during Early Mississippian (ca. 340 Ma). Modified from Blakey (2010 website).

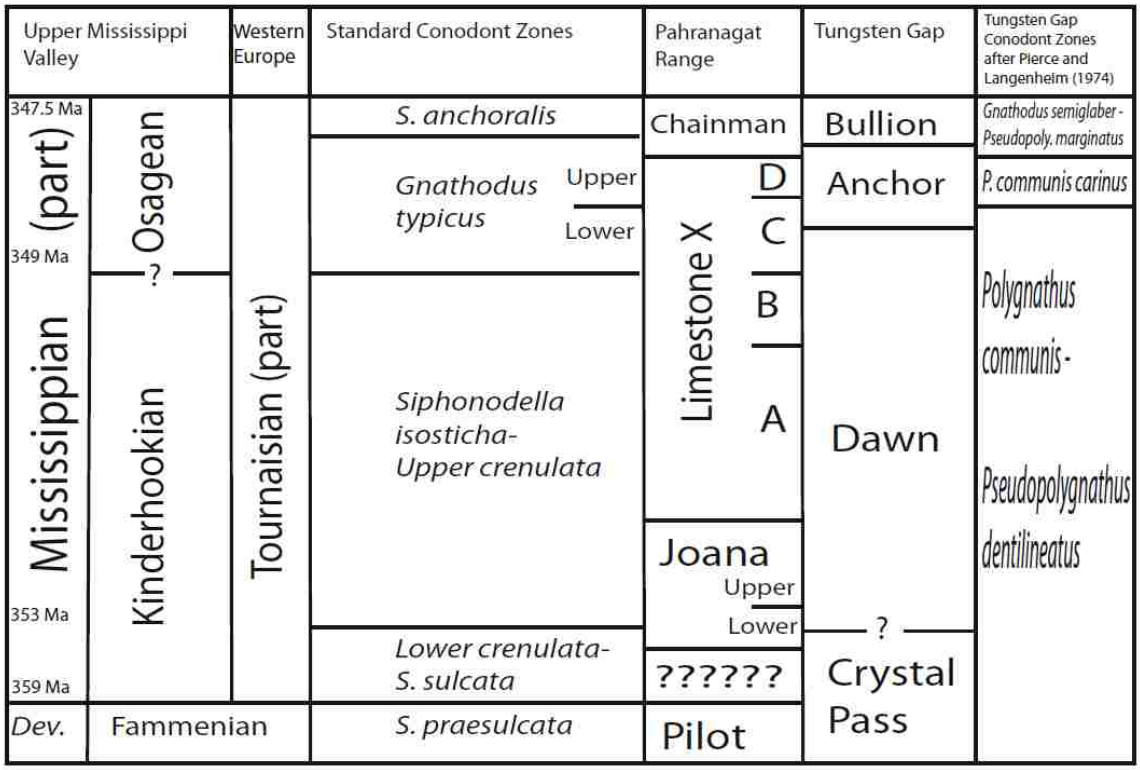

Figure 3. Stratigraphic nomenclature and conodont zones for the Alamo section in Pahranagat Range and the Tungsten Gap section in Arrow Canyon modified from Saltzman (2002). Note that because the lowermost conodont zones were not found in the Alamo section, previous studies suggest a stratigraphic gap (Saltzman et al., 2000; Saltzman, 2002). However, in the measured section, the change from the Pilot Shale to the Joana Limestone is transitional with increased limestone layers upward to massive limestone. The missing conodont zones may be the result of poor fossil preservation. Conodont zonations for Tungsten Gap section are from Pierce (1969) and Pierce and Langenheim (1974). Numerical ages are from Buggisch et al. (2008).

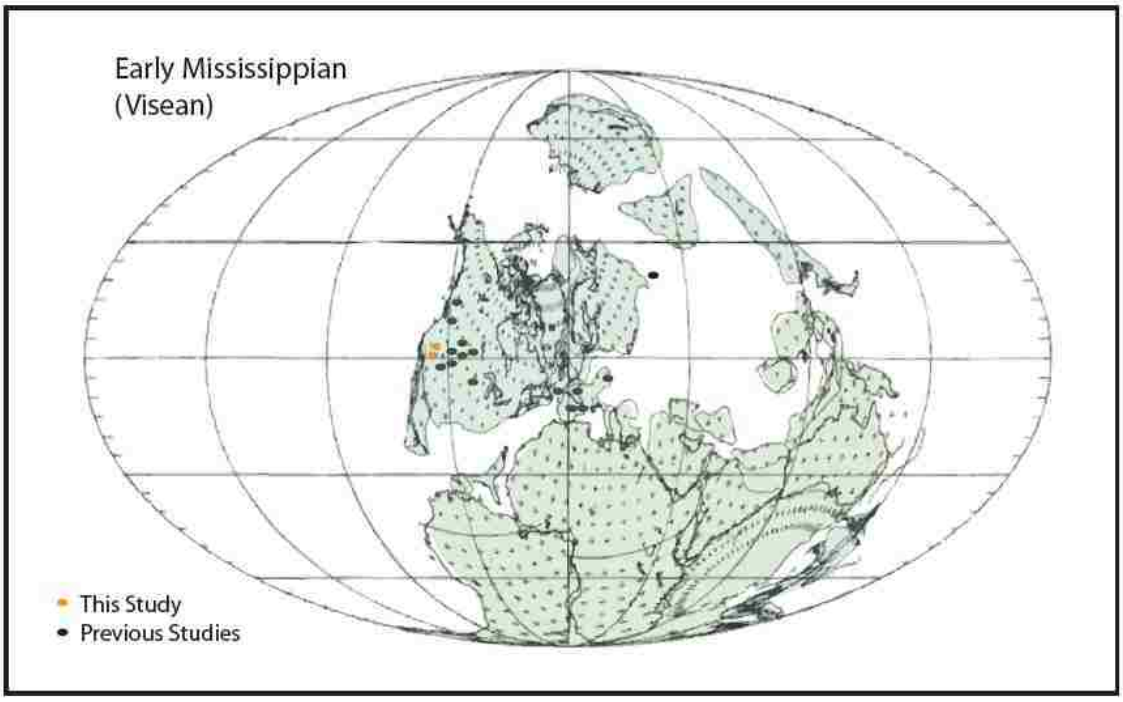

Figure 4. Global paleoreconstruction of the Early Mississippian continents, showing approximate paleolocalities of existing documentations of the Early Mississippian $\delta^{13}C_{carb}$ excursion. Modified from Scotese and McKerrow (1990).

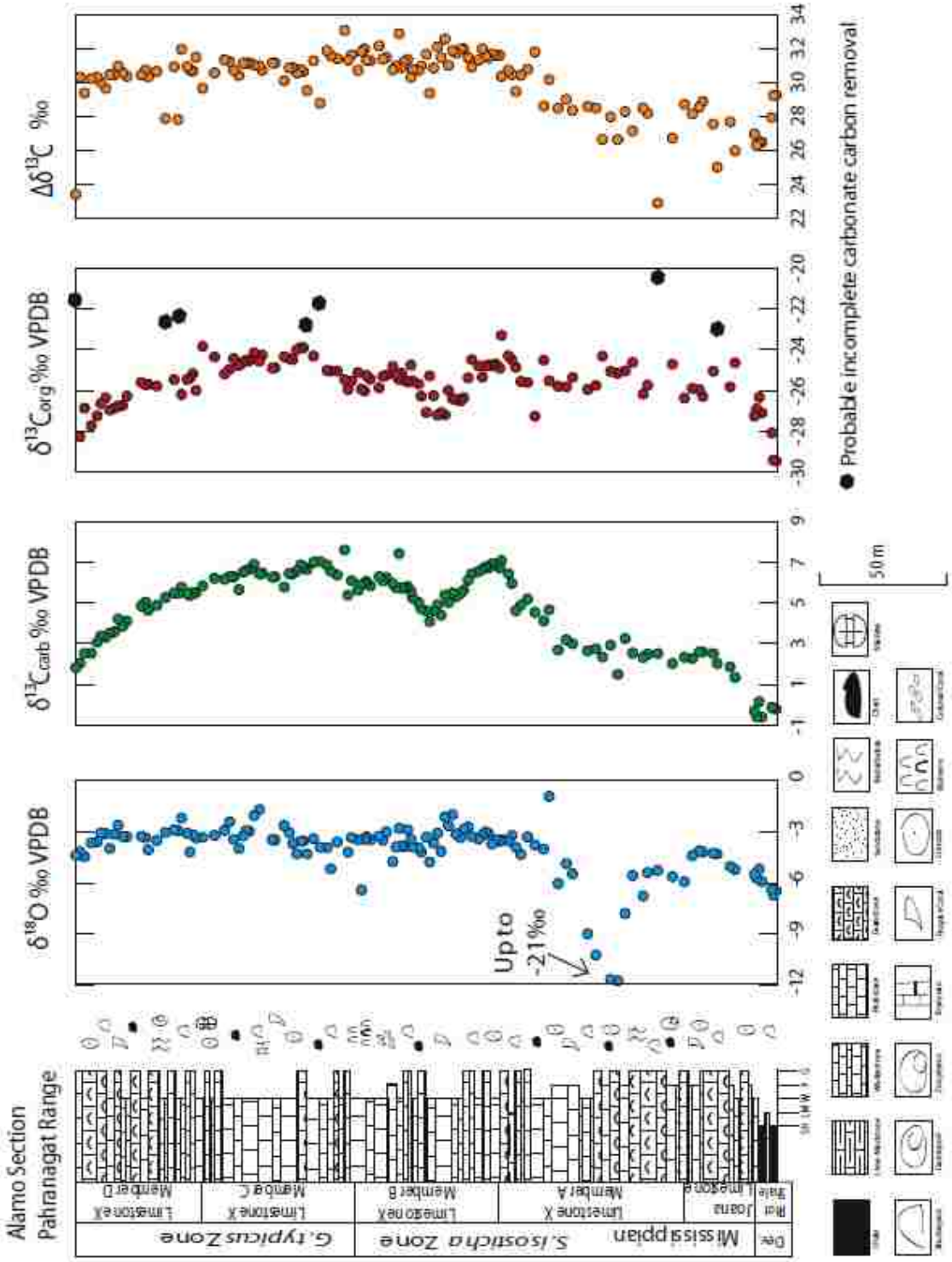

Figure 5. Stratigraphy and isotope profiles of $\delta^{13}C_{carb}$, $\delta^{13}C_{org}$, $\delta^{18}O$, and $\Delta\delta^{13}C$ from the Alamo section in the Pahranagat Range, Nevada.

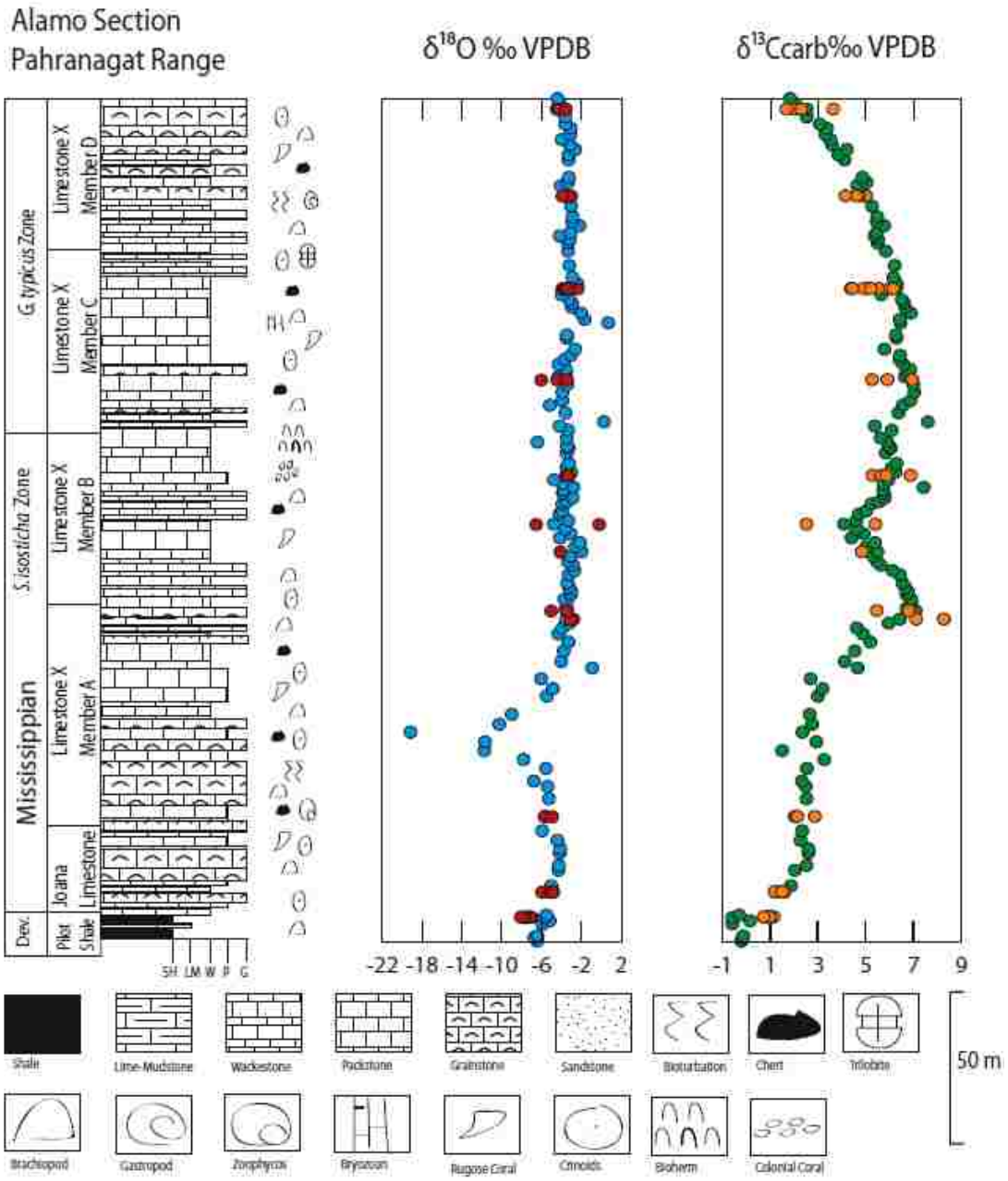

Figure 6. Stratigraphy and $\delta^{13}C_{carb}$ and $\delta^{18}O$ profiles that include brachiopod data (orange and red dots, respectively) from the Alamo section in the Pahranagat Range, Nevada.

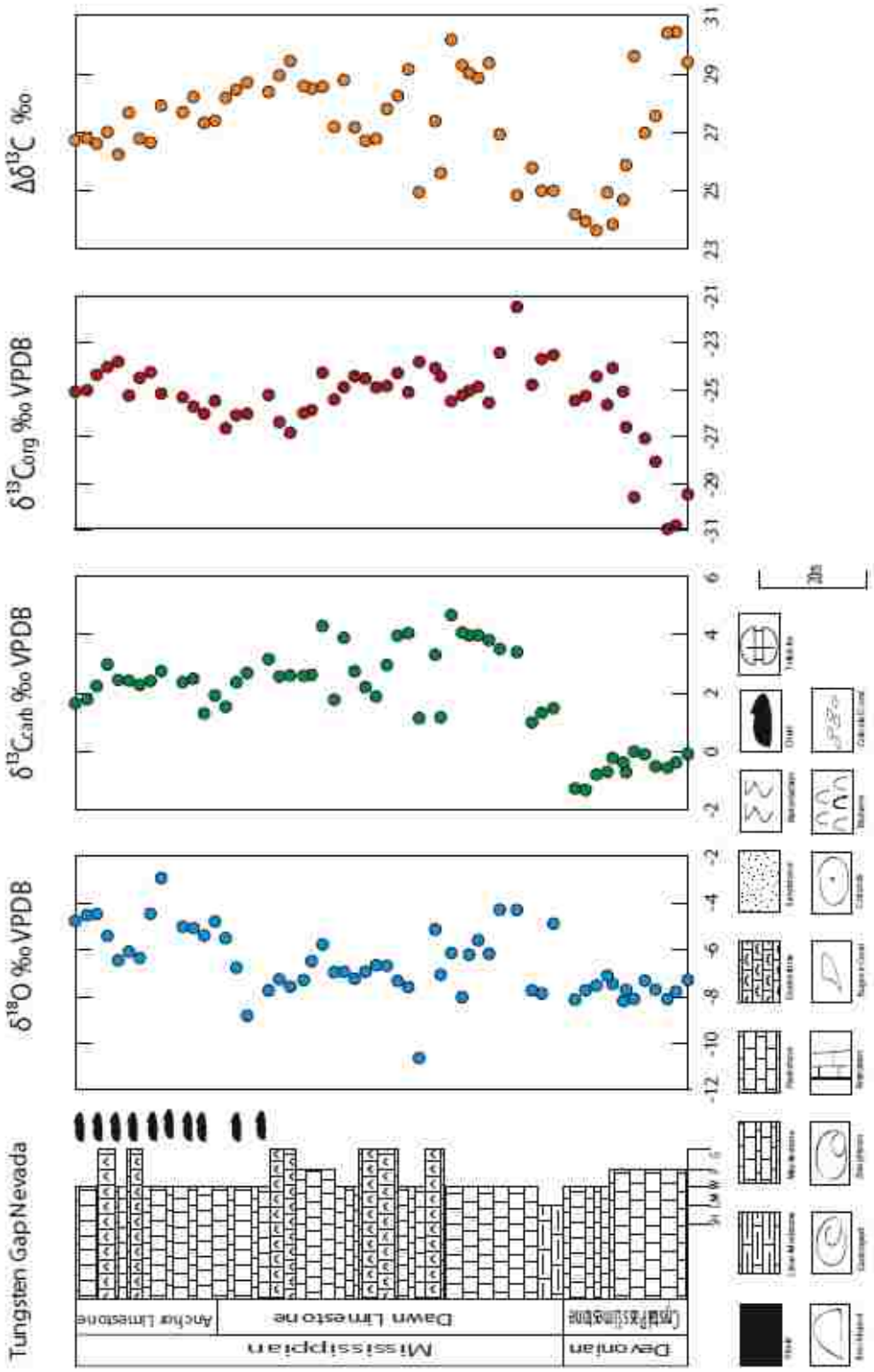

Figure 7. Stratigraphy and isotope profiles ($\delta^{13}C_{carb}$, $\delta^{13}C_{org}$, $\delta^{18}O$, and $\Delta\delta^{13}C$) from the Tungsten Gap section in Arrow Canyon, southeastern Nevada.

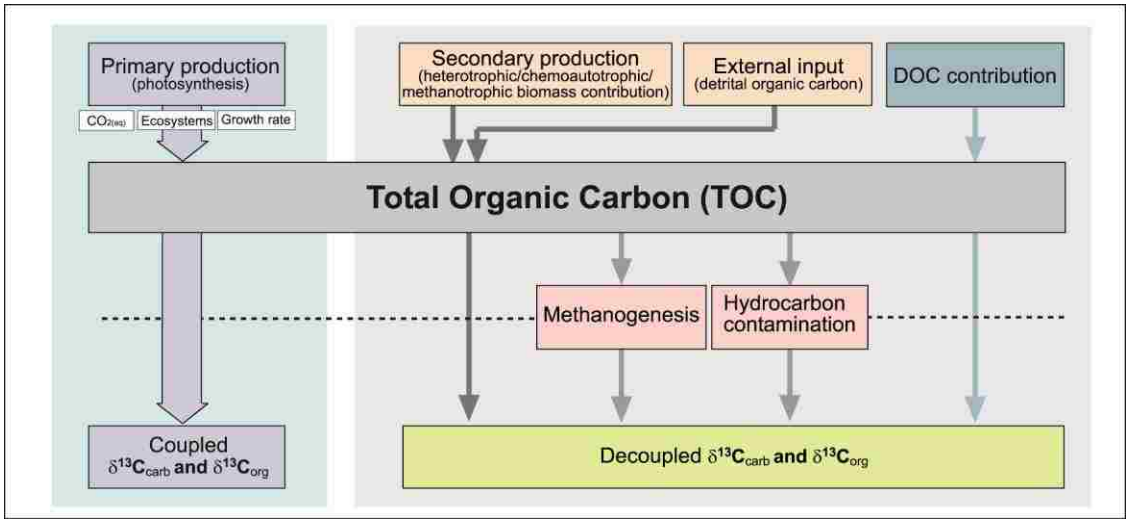

Figure 8. Schematic diagram showing the controlling factors that can potentially control the $\delta^{13}C$ of bulk organic matter. The overall coupled (covarying) $\delta^{13}C_{carb}$ and $\delta^{13}C_{org}$ trends from the Alamo section indicate that the majority of organic carbon contribution was from photosynthetic carbon fixation (primary production). However, the decoupled (variable) $\delta^{13}C_{carb}$ and $\delta^{13}C_{org}$ from the Tungsten Gap section may not have a unique origin. It may have resulted from frequent changes in meteoric water input that would have changed the $\delta^{13}C$ value of primary organic matter, detrital organic carbon contribution in more proximal shelf environments, or diagenetic modification (methanogenesis) that have changed both $\delta^{13}C_{carb}$ and $\delta^{13}C_{org}$ values. Diagenetic alteration is the most valid of these options for the Tungsten Gap section.

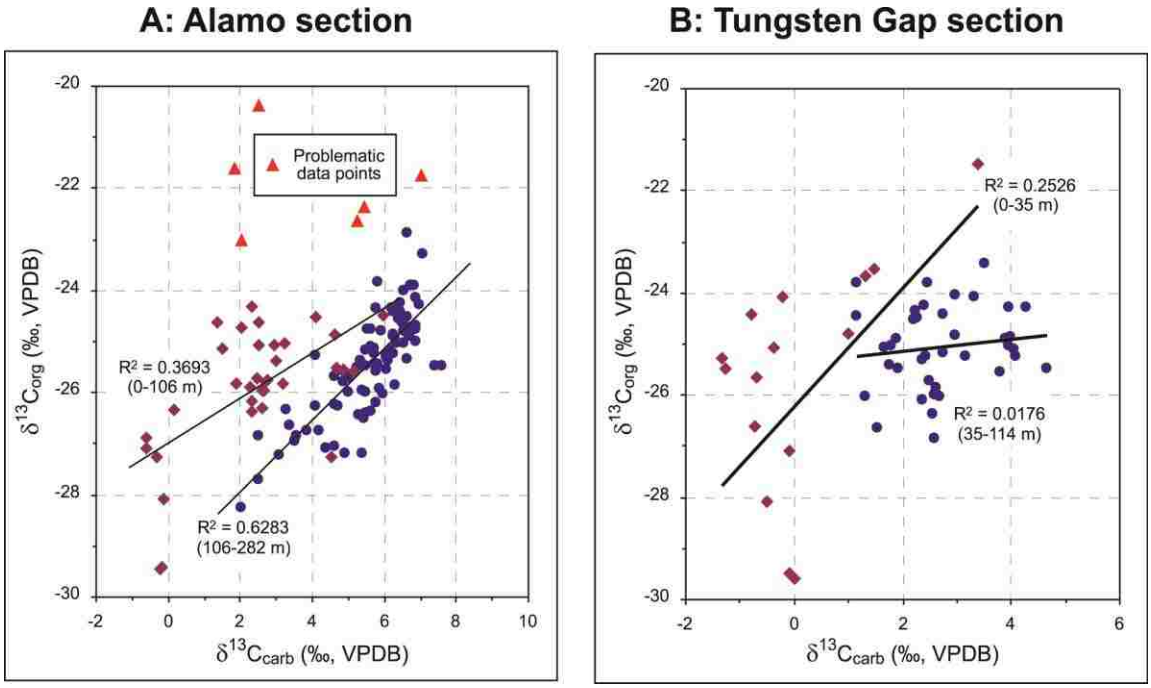

Figure 9. Cross plots of $\delta^{13}C_{carb}$ and $\delta^{13}C_{org}$ for the Alamo section (A) and the Tungsten Gap section (B). Notice that there are a few data points (red triangles) that are questionable because these values departure abruptly and significantly from their adjacent samples thus, they are suspected to have been contaminated by incomplete carbonate removal during analyses and need to be reanalyzed in the future. The better correlation between $\delta^{13}C_{carb}$ and $\delta^{13}C_{org}$ in the Alamo section implies that primary production contributed to the majority of organic carbon, whereas the lack of $\delta^{13}C_{carb}$ and $\delta^{13}C_{org}$ covariation in the Tungsten Gap section suggests detrital organic carbon contribution or diagenetic modification on $\delta^{13}C_{carb}$, $\delta^{13}C_{org}$, or both.

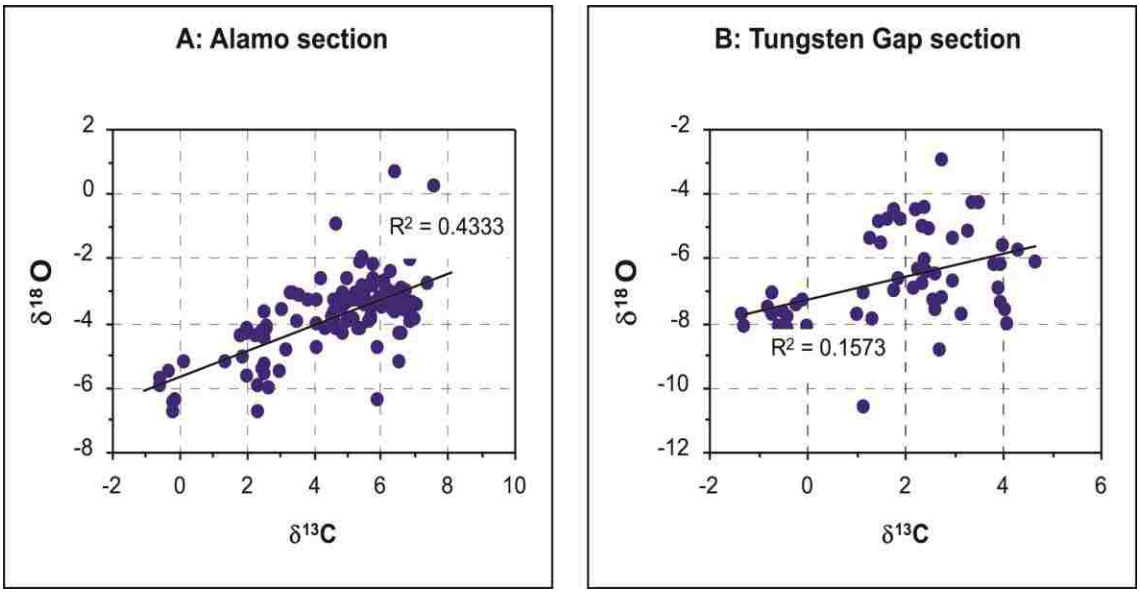

Figure 10. Cross plots of $\delta^{13}C_{carb}$–$\delta^{18}O$ of the Alamo section (A) and Tungsten Gap section (B).

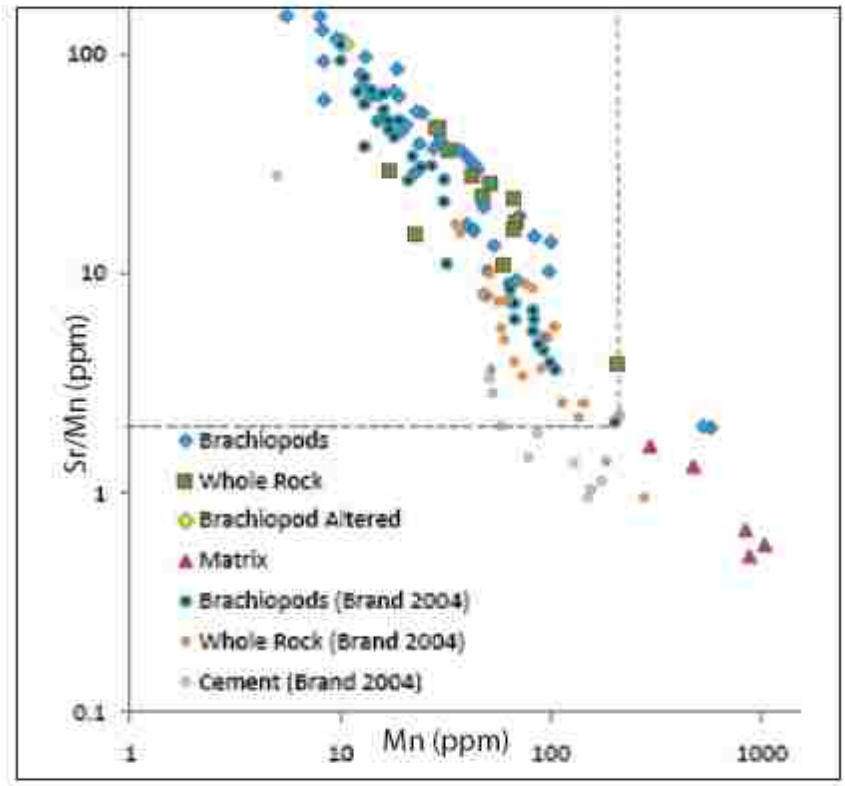

Figure 11. Sr/Mn ratios and Mn contents of brachiopods, whole rock, and matrix from the Alamo section in Pahranagat Range. Brachiopod, whole rock, and cement results from Brand (2004) also are included on the plot. Dashed line indicates the limits for retention of original seawater Sr isotopes ($\geq$ 2.0 Sr/Mn) and $\leq$ 300 mg/kg for Mn in whole rock limestone (Brand, 2004; Denison et al., 1994). Most of the brachiopod samples analyzed in this study fall in the region of potential chemical retention.

APPENDIX I

Stratigraphic unit	Sample No.	Strat. Height	Lithology	$\delta^{13}C$	$\delta^{18}O$	TOC%	$\delta^{13}C_{org}$	$\Delta\delta$
Pahranagat Range near Alamo, Nevada				(‰, VPDB)	(‰, VPDB)		(‰, VPDB)	
Pilot Shale	AL - 0.3	0.30	Shaley Lime-Mudstone	-0.21	-6.45	0.220	-29.46	29.25
Pilot Shale	AL - 1.4	1.40	Shaley Lime-Mudstone	-0.17	-6.73	0.230	-29.41	29.24
Pilot Shale	AL - 2.05	2.05	Wackestone	-0.13	-6.40	0.052	-28.08	27.95
Pilot Shale	AL - 6.0	6.00	Grainstone	-0.80	-5.93	0.060	-27.10	26.30
Pilot Shale	AL - 7.1	7.10	Grainstone	0.15	-5.19	0.039	-26.33	26.48
Pilot Shale	AL - 8.1	8.10	Wackestone	-0.60	-5.73	0.051	-26.90	26.29
Pilot Shale	AL - 9	9.00	Wackestone	-0.30	-5.50	0.064	-27.25	26.95
Joana Limestone	AL - 16.8	16.80	Grainstone	1.34	-5.22	0.049	-24.64	25.98
Joana Limestone	AL - 18.8	18.80	Grainstone	1.86	-5.04	0.044	-25.82	27.69
Joana Limestone	AL - 24	24.00	Packstone	2.02	-4.31	0.047	-23.00	25.02
Joana Limestone	AL - 25.6	25.60	Grainstone	2.51	-4.27	0.054	-25.05	27.56
Joana Limestone	AL - 29.8	29.80	Grainstone	2.59	-4.19	0.051	-26.29	28.88
Joana Limestone	AL - 31.2	31.20	Grainstone	2.59	-4.13	0.048	-25.96	28.55
Joana Limestone	AL - 34	34.00	Grainstone	2.26	-4.41	0.043	-25.89	28.15
Limestone X Mbr. A	AL - 37.2	37.20	Grainstone	2.33	-5.94	0.057	-26.37	28.70
Limestone X Mbr. A	AL - 42	42.00	Grainstone	2.02	-5.65	0.066	-24.71	26.73
Limestone X Mbr. A	AL - 47.9	47.90	Packstone	2.51	-5.27	0.045	-20.39	22.90
Limestone X Mbr. A	AL - 52	52.00	Grainstone	2.48	-5.40	0.065	-25.73	28.20
Limestone X Mbr. A	AL - 53.8	53.80	Grainstone	2.32	-6.78	0.064	-26.17	28.49
Limestone X Mbr. A	AL - 58.05	58.05	Grainstone	2.53	-5.57	0.056	-24.62	27.15
Limestone X Mbr. A	AL - 61	61.00	Packstone	3.25	-7.01	0.048	-25.04	28.28
Limestone X Mbr. A	AL - 64	64.00	Grainstone	1.49	-11.76	0.040	-25.15	26.64
Limestone X Mbr. A	AL - 66.9	66.90	Grainstone	2.92	-11.68	0.045	-25.06	27.98
Limestone X Mbr. A	AL - 70.2	70.20	Packstone	2.34	-10.18	0.028	-24.31	26.65
Limestone X Mbr. A	AL - 72.8	72.80	Wackestone	2.74	-10.25	0.057	-25.75	28.49
Limestone X Mbr. A	AL - 76.1	76.10	Wackestone	2.64	-9.00	0.038	-25.95	28.59
Limestone X Mbr. A	AL - 82.2	82.20	Wackestone	2.99	-5.47	0.041	-25.36	28.35
Limestone X Mbr. A	AL - 84.7	84.70	Packstone	3.18	-4.87	0.045	-25.82	29.00
Limestone X Mbr. A	AL - 88	88.00	Packstone	2.68	-6.04	0.025	-25.79	28.48
Limestone X Mbr. A	AL - 91.6	91.60	Packstone	4.65	-0.92	0.022	-25.52	30.16
Limestone X Mbr. A	AL - 93.8	93.80	Packstone	4.11	-4.02	0.057	-24.51	28.61
Limestone X Mbr. A	AL - 97.3	97.30	Wackestone	4.53	-3.78	0.157	-27.26	31.79
Limestone X Mbr. A	AL - 100.3	100.30	Wackestone	5.18	-3.30	0.104	-25.60	30.77
Limestone X Mbr. A	AL - 103	103.00	Wackestone	4.88	-4.33	0.122	-25.55	30.43
Limestone X Mbr. A	AL - 105	105.00	Wackestone	4.61	-3.90	0.086	-24.86	29.47
Limestone X Mbr. A	AL - 106.6	106.60	Wackestone	5.95	-3.22	0.098	-24.50	30.46
Limestone X Mbr. A	AL - 108	108.00	Wackestone	6.42	-3.54	0.119	-24.30	30.72
Limestone X Mbr. B	AL - 110.8	110.80	Wackestone	7.07	-3.45	0.094	-23.29	30.36
Limestone X Mbr. B	AL - 111.5	111.50	Lime-Mudstone	6.70	-3.58	0.209	-24.90	31.60
Limestone X Mbr. B	AL - 113.1	113.10	Lime-Mudstone	6.90	-3.48	0.151	-24.69	31.59
Limestone X Mbr. B	AL - 114.6	114.60	Wackestone	6.90	-3.72	0.146	-24.77	31.67
Limestone X Mbr. B	AL - 116.1	116.10	Wackestone	6.70	-3.09	0.162	-24.74	31.44
Limestone X Mbr. B	AL - 117.2	117.20	Wackestone	6.75	-3.01	0.134	-24.81	31.56
Limestone X Mbr. B	AL - 118.5	118.50	Wackestone	6.64	-3.23	0.147	-25.34	31.98

Limestone X Mbr. B	AL-120	120.00	Wackestone	6.53	-3.43	0.151	-24.79	31.31
Limestone X Mbr. B	AL-122.8	122.80	Wackestone	6.42	-3.27	0.129	-24.48	30.91
Limestone X Mbr. B	AL-124.2	124.20	Grainstone	6.11	-2.71	0.067	-25.38	31.48
Limestone X Mbr. B	AL-126	126.00	Wackestone	5.62	-2.85	0.145	-26.35	31.98
Limestone X Mbr. B	AL-127.2	127.20	Wackestone	5.46	-3.35	0.174	-26.50	31.96
Limestone X Mbr. B	AL-129	129.00	Wackestone	5.29	-3.12	0.125	-26.43	31.72
Limestone X Mbr. B	AL-130.5	130.50	Wackestone	5.48	-1.99	0.098	-26.40	31.87
Limestone X Mbr. B	AL-132.1	132.10	Wackestone	5.01	-2.64	0.258	-25.99	31.01
Limestone X Mbr. B	AL-133.5	133.50	Wackestone	5.37	-2.13	0.199	-27.19	32.56
Limestone X Mbr. B	AL-135.1	135.10	Wackestone	4.39	-4.15	0.170	-27.08	31.47
Limestone X Mbr. B	AL-136.5	136.50	Wackestone	4.90	-3.08	0.202	-27.20	32.10
Limestone X Mbr. B	AL-138.1	138.10	Wackestone	4.60	-3.66	0.078	-26.25	30.85
Limestone X Mbr. B	AL-139.7	139.70	Wackestone	4.08	-4.78	0.085	-25.20	29.37
Limestone X Mbr. B	AL-141	141.00	Wackestone	4.60	-3.51	0.074	-27.07	31.67
Limestone X Mbr. B	AL-143.1	143.10	Grainstone	4.70	-4.20	0.111	-26.27	30.97
Limestone X Mbr. B	AL-144.1	144.10	Grainstone	5.01	-3.94	0.096	-25.68	30.69
Limestone X Mbr. B	AL-146.5	146.50	Grainstone	5.23	-3.91	0.082	-25.53	30.75
Limestone X Mbr. B	AL-147.2	147.20	Grainstone	5.55	-3.45	0.086	-24.75	30.30
Limestone X Mbr. B	AL-148.5	148.50	Grainstone	5.79	-2.88	0.099	-25.58	31.36
Limestone X Mbr. B	AL-150	150.00	Grainstone	5.75	-3.87	0.130	-25.48	31.21
Limestone X Mbr. B	AL-151	151.00	Wackestone	5.72	-3.82	0.092	-25.15	30.87
Limestone X Mbr. B	AL-152	152.00	Packstone	7.41	-2.74	0.101	-25.46	32.87
Limestone X Mbr. B	AL-153.2	153.20	Packstone	5.74	-3.89	0.134	-25.23	30.97
Limestone X Mbr. B	AL-154.5	154.50	Wackestone	5.94	-4.75	0.077	-24.81	30.75
Limestone X Mbr. B	AL-157.1	157.10	Wackestone	6.24	-3.01	0.249	-25.25	31.49
Limestone X Mbr. B	AL-158.5	158.50	Wackestone	6.07	-3.49	0.073	-25.30	31.37
Limestone X Mbr. B	AL-160	160.00	Wackestone	6.28	-3.26	0.480	-25.87	32.15
Limestone X Mbr. B	AL-163.5	163.50	Wackestone	5.83	-3.47	0.123	-25.44	31.28
Limestone X Mbr. B	AL-165.1	165.10	Wackestone	6.04	-3.29	0.124	-25.26	31.31
Limestone X Mbr. B	AL-165.9	165.90	Wackestone	5.96	-3.45	0.205	-25.02	31.98
Limestone X Mbr. B	AL-167.1	167.10	Wackestone	5.89	-6.42	0.098	-25.93	31.82
Limestone X Mbr. C	AL-168.5	168.50	Wackestone	5.61	-3.47	0.165	-25.12	30.72
Limestone X Mbr. C	AL-171.1	171.10	Wackestone	6.08	-3.34	0.151	-25.53	31.61
Limestone X Mbr. C	AL-172.5	172.50	Wackestone	5.87	-4.20	0.135	-25.95	31.52
Limestone X Mbr. C	AL-173.9	173.90	Grainstone	7.59	0.26	0.110	-25.47	33.06
Limestone X Mbr. C	AL-176.9	176.90	Grainstone	6.36	-3.60	0.171	-25.04	31.40
Limestone X Mbr. C	AL-179.5	179.50	Wackestone	6.55	-5.18	0.119	-25.04	31.58
Limestone X Mbr. C	AL-181	181.00	Wackestone	6.86	-3.93	0.157	-25.01	31.87
Limestone X Mbr. C	AL-183.8	183.80	Wackestone	7.02	-3.91	0.058	-21.76	28.78
Limestone X Mbr. C	AL-186.4	186.40	Wackestone	6.98	-3.40	0.071	-24.30	31.28
Limestone X Mbr. C	AL-189	189.00	Wackestone	6.63	-4.30	0.065	-22.89	29.52
Limestone X Mbr. C	AL-190.5	190.50	Wackestone	6.74	-3.54	0.083	-23.90	30.65
Limestone X Mbr. C	AL-191.5	191.50	Wackestone	6.85	-3.55	0.078	-23.90	30.75
Limestone X Mbr. C	AL-193.1	193.10	Wackestone	6.56	-4.29	0.111	-24.00	30.56
Limestone X Mbr. C	AL-194.8	194.80	Wackestone	6.41	-3.48	0.111	-24.48	30.89
Limestone X Mbr. C	AL-196.2	196.20	Wackestone	6.43	-3.05	0.084	-24.42	30.85

Limestone X Mbr. C	AL - 198.2	198.20	Wackestone	5.77	-2.63	0.040	-24.34	30.10
Limestone X Mbr. C	AL - 201.9	201.90	Wackestone	6.27	-3.48	0.116	-24.88	31.15
Limestone X Mbr. C	AL - 203	203.00	Wackestone	6.25	-3.46	0.114	-24.90	31.15
Limestone X Mbr. C	AL - 207	207.00	Wackestone	6.45	-0.69	0.084	-24.26	30.71
Limestone X Mbr. C	AL - 208.2	208.20	Wackestone	6.41	-1.69	0.120	-24.56	30.98
Limestone X Mbr. C	AL - 210.3	210.30	Wackestone	6.66	-2.04	0.080	-24.15	31.03
Limestone X Mbr. C	AL - 212.2	212.20	Wackestone	6.64	-2.97	0.095	-24.53	31.17
Limestone X Mbr. C	AL - 213.5	213.50	Wackestone	6.60	-2.94	0.071	-24.51	31.11
Limestone X Mbr. C	AL - 214.7	214.70	Wackestone	6.50	-3.24	0.091	-24.62	31.12
Limestone X Mbr. C	AL - 216.4	216.40	Wackestone	5.64	-3.98	0.071	-24.77	30.41
Limestone X Mbr. C	AL - 218.5	218.50	Wackestone	6.27	-3.44	0.062	-24.43	30.71
Limestone X Mbr. C	AL - 220.1	220.10	Wackestone	6.29	-2.41	0.086	-24.95	31.25
Limestone X Mbr. C	AL - 222.2	222.20	Wackestone	6.15	-2.91	0.092	-25.18	31.33
Limestone X Mbr. D	AL - 226.2	226.20	Wackestone	6.20	-3.21	0.061	-24.35	30.56
Limestone X Mbr. D	AL - 231	231.00	Wackestone	5.83	-3.33	0.103	-23.83	29.66
Limestone X Mbr. D	AL - 233.7	233.70	Wackestone	5.49	-3.36	0.108	-25.99	31.48
Limestone X Mbr. D	AL - 234.9	234.90	Wackestone	5.50	-3.17	0.096	-25.17	30.67
Limestone X Mbr. D	AL - 236.1	236.10	Wackestone	5.35	-4.19	0.090	-25.38	30.73
Limestone X Mbr. D	AL - 237.2	237.20	Wackestone	5.46	-3.09	0.039	-25.46	30.93
Limestone X Mbr. D	AL - 239.5	239.50	Wackestone	5.76	-2.20	0.039	-26.19	31.95
Limestone X Mbr. D	AL - 240.9	240.90	Wackestone	5.45	-2.93	0.158	-22.36	27.82
Limestone X Mbr. D	AL - 242.5	242.50	Grainstone	5.47	-2.89	0.030	-25.46	30.93
Limestone X Mbr. D	AL - 246	246.00	Grainstone	5.25	-3.04	0.055	-22.63	27.88
Limestone X Mbr. D	AL - 249.5	249.50	Grainstone	4.87	-3.51	0.075	-25.78	30.65
Limestone X Mbr. D	AL - 252.9	252.90	Grainstone	4.63	-4.06	0.076	-25.69	30.32
Limestone X Mbr. D	AL - 254	254.00	Grainstone	5.05	-3.35	0.071	-25.71	30.74
Limestone X Mbr. D	AL - 255.7	255.70	Wackestone	4.85	-3.26	0.047	-25.60	30.45
Limestone X Mbr. D	AL - 261.5	261.50	Wackestone	4.10	-3.29	0.047	-26.27	30.37
Limestone X Mbr. D	AL - 263.2	263.20	Grainstone	3.85	-3.28	0.055	-26.73	30.58
Limestone X Mbr. D	AL - 265	265.00	Wackestone	4.20	-2.62	0.046	-26.76	30.96
Limestone X Mbr. D	AL - 266.5	266.50	Grainstone	3.58	-3.15	0.064	-26.86	30.44
Limestone X Mbr. D	AL - 268.3	268.30	Grainstone	3.51	-3.98	0.064	-26.95	30.46
Limestone X Mbr. D	AL - 270	270.00	Wackestone	3.30	-3.11	0.047	-26.35	29.65
Limestone X Mbr. D	AL - 272	272.00	Wackestone	3.37	-3.07	0.054	-26.64	30.00
Limestone X Mbr. D	AL - 273.4	273.40	Wackestone	3.07	-3.60	0.075	-27.24	30.31
Limestone X Mbr. D	AL - 275.8	275.80	Grainstone	2.52	-3.64	0.057	-27.71	30.23
Limestone X Mbr. D	AL - 278.5	278.50	Grainstone	2.52	-4.46	0.042	-26.86	29.38
Limestone X Mbr. D	AL - 280.3	280.30	Grainstone	2.04	-4.17	0.072	-28.27	30.31
Limestone X Mbr. D	AL - 282	282.00	Grainstone	1.82	-4.39	0.191	-21.60	23.42
Tungsten Gap, Nevada								
Crystal Pass Limestone	TG - 118	0.00	Packstone	-0.08	-7.29	0.055	-29.48	29.40
Crystal Pass Limestone	TG - 120.2	2.20	Packstone	-0.38	-7.79	0.038	-30.81	30.43
Crystal Pass Limestone	TG - 121.8	3.80	Packstone	-0.56	-8.10	0.044	-30.96	30.40
Crystal Pass Limestone	TG - 124	6.00	Packstone	-0.51	-7.70	0.020	-28.08	27.56
Crystal Pass Limestone	TG - 126	8.00	Packstone	-0.10	-7.32	0.066	-27.08	26.98

Crystal Pass Limestone	TG - 128	10.00	Packstone	0.00	-8.10	0.044	-29.60	29.60
Crystal Pass Limestone	TG - 129.5	11.50	Packstone	-0.71	-7.71	0.034	-26.50	25.08
Crystal Pass Limestone	TG - 130	12.00	Packstone	-0.38	-8.19	0.017	-25.08	24.69
Crystal Pass Limestone	TG - 132	14.00	Wackestone	-0.22	-7.46	0.015	-24.07	23.85
Crystal Pass Limestone	TG - 133	15.00	Wackestone	-0.70	-7.11	0.014	-25.64	24.94
Crystal Pass Limestone	TG - 135	17.00	Wackestone	-0.79	-7.52	0.023	-24.45	23.64
Crystal Pass Limestone	TG - 137	19.00	Lime-Mudstone	-1.32	-7.73	0.014	-25.27	23.95
Crystal Pass Limestone	TG - 139	21.00	Lime-Mudstone	-1.27	-8.13	0.018	-25.46	24.19
Dawn Limestone	TG - 143	25.00	Wackestone	1.48	-4.88	0.018	-23.52	25.00
Dawn Limestone	TG - 145.2	27.20	Packstone	1.32	-7.87	0.023	-23.68	25.00
Dawn Limestone	TG - 147	29.00	Packstone	1.00	-7.73	0.027	-24.79	25.79
Dawn Limestone	TG - 149.8	31.80	Packstone	3.40	-4.29	0.022	-23.46	24.85
Dawn Limestone	TG - 153	35.00	Wackestone	3.51	-4.28	0.031	-23.42	26.93
Dawn Limestone	TG - 155	37.00	Wackestone	3.81	-6.17	0.043	-25.56	29.37
Dawn Limestone	TG - 157	39.00	Wackestone	3.98	-5.59	0.046	-24.88	28.86
Dawn Limestone	TG - 158.7	40.70	Wackestone	3.97	-6.20	0.042	-25.05	29.02
Dawn Limestone	TG - 160	42.00	Wackestone	4.07	-8.02	0.057	-25.23	29.30
Dawn Limestone	TG - 163	44.00	Packstone	4.67	-6.13	0.058	-25.49	30.17
Dawn Limestone	TG - 164	46.00	Packstone	1.17	-7.06	0.043	-24.44	25.61
Dawn Limestone	TG - 165	47.00	Packstone	3.31	-5.13	0.044	-24.07	27.38
Dawn Limestone	TG - 168	50.00	Grainstone	1.14	-10.63	0.044	-23.81	24.95
Dawn Limestone	TG - 170	52.00	Grainstone	4.05	-7.59	0.066	-25.11	29.16
Dawn Limestone	TG - 172	54.00	Packstone	3.96	-7.33	0.071	-24.29	28.25
Dawn Limestone	TG - 174	56.00	Packstone	2.96	-6.68	0.060	-24.84	27.80
Dawn Limestone	TG - 176	58.00	Grainstone	1.88	-6.66	0.048	-24.90	26.78
Dawn Limestone	TG - 178	60.00	Grainstone	2.20	-6.83	0.047	-24.52	26.71
Dawn Limestone	TG - 180	62.00	Grainstone	2.75	-7.24	0.046	-24.42	27.17
Dawn Limestone	TG - 182	64.00	Grainstone	3.89	-6.95	0.051	-24.90	28.79
Dawn Limestone	TG - 183.8	65.80	Wackestone	1.77	-6.96	0.060	-25.42	27.19
Dawn Limestone	TG - 186	68.00	Packstone	4.29	-5.77	0.054	-24.27	28.56
Dawn Limestone	TG - 188	70.00	Packstone	2.62	-6.48	0.054	-25.87	28.49
Dawn Limestone	TG - 189.5	71.50	Packstone	2.59	-7.29	0.078	-26.00	28.59
Dawn Limestone	TG - 192	74.00	Packstone	2.60	-7.57	0.102	-26.64	29.44
Dawn Limestone	TG - 194	76.00	Packstone	2.57	-7.26	0.070	-26.38	28.95
Dawn Limestone	TG - 196	78.00	Grainstone	3.16	-7.74	0.054	-25.22	28.38
Dawn Limestone	TG - 200	82.00	Grainstone	2.69	-8.82	0.045	-26.02	28.71
Dawn Limestone	TG - 202	84.00	Grainstone	2.37	-6.76	0.041	-26.09	28.46
Dawn Limestone	TG - 204	86.00	Grainstone	1.53	-5.50	0.057	-26.65	28.18
Anchor Limestone	TG - 206	88.00	Grainstone	1.92	-4.79	0.032	-25.48	27.40
Anchor Limestone	TG - 208	90.00	Wackestone	1.30	-5.38	0.043	-26.02	27.32
Anchor Limestone	TG - 210	92.00	Wackestone	2.49	-5.07	0.051	-25.72	28.21
Anchor Limestone	TG - 212	94.00	Wackestone	2.37	-5.01	0.053	-25.32	27.69
Anchor Limestone	TG - 216	98.00	Wackestone	2.75	-2.93	0.030	-25.16	27.91
Anchor Limestone	TG - 218	100.00	Wackestone	2.41	-4.45	0.026	-24.25	26.65
Anchor Limestone	TG - 220	102.00	Wackestone	2.28	-6.35	0.022	-24.49	26.78
Anchor Limestone	TG - 222	104.00	Wackestone	2.42	-6.08	0.029	-25.25	27.67
Anchor Limestone	TG - 224	106.00	Wackestone	2.45	-6.45	0.025	-23.80	26.25
Anchor Limestone	TG - 226	108.00	Grainstone	2.98	-5.40	0.028	-24.03	27.01
Anchor Limestone	TG - 228	110.00	Grainstone	2.24	-4.47	0.025	-24.36	26.61
Anchor Limestone	TG - 229.8	111.80	Grainstone	1.78	-4.52	0.029	-25.02	26.80
Anchor Limestone	TG - 232	114.00	Grainstone	1.65	-4.77	0.037	-25.06	26.73

APPENDIX II

Sample #	Location	Notes/Host rx	δ13C	δ18O	Ca	Mg	Sr	Fe	Mn
Pilot Shale (PS)									
B3-1M	matrix	PS, ~1m below cont	0.37	-3.94	340261	54739	604	1349	1035
B3-2	brach frag	"	0.79	-7.81	393444	1556	1339	36	45
B3-3	brach frag	"	1.06	-7.55	393410	1590	1363	31	44
B3-4	brach frag	"	1.01	-7.50	393563	1437	1370	36	37
B3-5m1	matrix-shale	PS, ~0.8m below co	0.11	-9.15	359852	35148	455	1289	879
B3-6m2	matrix-concretion	"	-0.61	-8.53	384745	10255	629	643	475
B3-7c	fract fill-cement	"	-5.10	-20.68	389066	5934	485	872	296
B3-8	brach frag	"	1.07	-7.30	393023	1978	1238	387	83
B3-9	brach frag-umbo	"	1.18	-7.03	394060	940	1396	110	100
B3-10	brach frag-umbo	"	1.02	-7.19	393886	1114	1372	119	40
B3-11	brach frag	"	1.00	-7.74					
B3-12	brach frag	"	0.78	-8.09					
B3-13m	whole rock	core; AL-16.8	1.94	-5.22	391914	3086	504	57	17
B3-14	brach frag, altered	"	1.18	<-4.84	393122	1878	1186	52	11
B3-15	brach frag	"	1.23	-5.96	394230	770	1688	47	8
B3-16	"	"	1.39	<-4.86	394126	874	1186	43	10
B3-17	"	"	1.33	-5.12	394043	957	830	33	6
B3-18	"	"	1.69	-5.05	394230	770	779	37	8
B3-19	"	"	1.53	-4.92	394158	842	522	27	8
B3-20m	whole rock	Lot X; AL-42	1.02	-5.65	392450	2550	345	56	22
B3-21	brach frag, altered	"	1.35	-5.44					
B3-22	brach frag	"	2.17	-5.69	392014	2986	1137	55	10
B3-23	"	"	1.90	<-4.83	394236	764	1198	29	8
B3-24m	whole rock	Lot X; AL-108	6.42	-3.54	391244	3756	1175	291	68
B3-25	brach frag	"	8.30	-2.80					
B3-26	"	"	7.14	-3.11	393961	1039	656	49	23
B3-27m	whole rock	Lot X; AL-110.8	7.07	-3.45	390110	4890	1325	252	51
B3-28	brach frag	"	8.48	-5.02					
B3-29	"	"	8.33	-3.49	390232	4768	1308	1682	71
B3-30m	whole rock	Lot X; AL-130.5	5.48	-1.99	389805	5195	1474	541	66
B3-31	brach frag	"	4.87	-4.11	386659	8341	1004	2910	98
B3-32m	whole rock	Lot X; AL-139.7	4.08	-4.76	391218	3782	1076	395	66
B3-33	brach frag	"	5.44	-0.21	387113	7887	1151	731	576
B3-34	"	"	3.55	-6.54	385701	9299	1067	1107	529
B3-35m	whole rock	Lot X; AL-156	6.59	-2.50	385428	9572	1350	127	29
B3-36c	cement	"	2.91	-7.26					
B3-37	brach frag	"	5.31	-9.55					
B3-38	"	"	5.67	-3.32	383808	11192	1364	36	42
B3-39	"	"	5.89	-3.37	392132	3868	1021	37	12
B3-40	"	"	6.91	-3.31	393158	1842	993	25	13

B3-41m	whole rock	Lst X; AL-188	5.57	-4.63	384653	10347	1204	60
B3-42	brach frag	"			389584	5416	1040	109
B3-43	"	"	5.94	-4.43	391780	3220	725	223
B3-44	"	"	5.29	-6.04	392478	2522	884	76
B3-45	"	"	6.98	-3.45				
B3-46m	whole rock	Lst X; AL-218.5	6.27	-3.44	390152	4848	1188	74
B3-47v	vein cement	"	7.04	-6.09	355387	39613	792	37
B3-48	brach frag	"	5.07	-3.65	384185	10815	1293	36
B3-49	"	"	4.95	-3.08	382071	12929	1277	98
B3-50	"	"	6.11	-2.37	384971	10029	1332	63
B3-51	"	"	5.56	-3.30	385568	9432	1269	95
B3-52	"	"	5.25	-3.53	382629	12371	1221	90
B3-53	"	"	6.04	-3.91	391690	3310	1605	63
B3-54	"	"	6.18	-3.75	388553	6447	1226	35
B3-55	"	"	4.41	-3.60	387876	7124	1228	34
B3-56	"	"	4.47	-3.36				
B3-57m	whole rock	Lst X; AL-249.5	4.87	-3.51	391897	3103	1077	69
B3-58	brach frag	"	5.03	-3.41				
B3-59	brach & cement	"	5.04	-3.21	393007	1993	932	35
B3-60	brach frag	"	4.74	-3.04	393236	1764	988	44
B3-61	"	"	4.65	-3.11				
B3-62	"	"	4.18	-3.92				
B3-63m	whole rock	Lst X; AL-278.5	2.52	-4.46	391333	3667	649	42
B3-64	brach frag	"	3.67	-4.36	392620	2380	978	98
B3-65	"	"	2.05	-3.78	392299	2701	682	36
B3-66	"	"	1.71	-4.27	390138	4862	644	63
B3-67	"	"	2.34	-3.55	392662	2338	673	64

APPENDIX III

Alamo Section in the Pahranagat Range detailed stratigraphic column

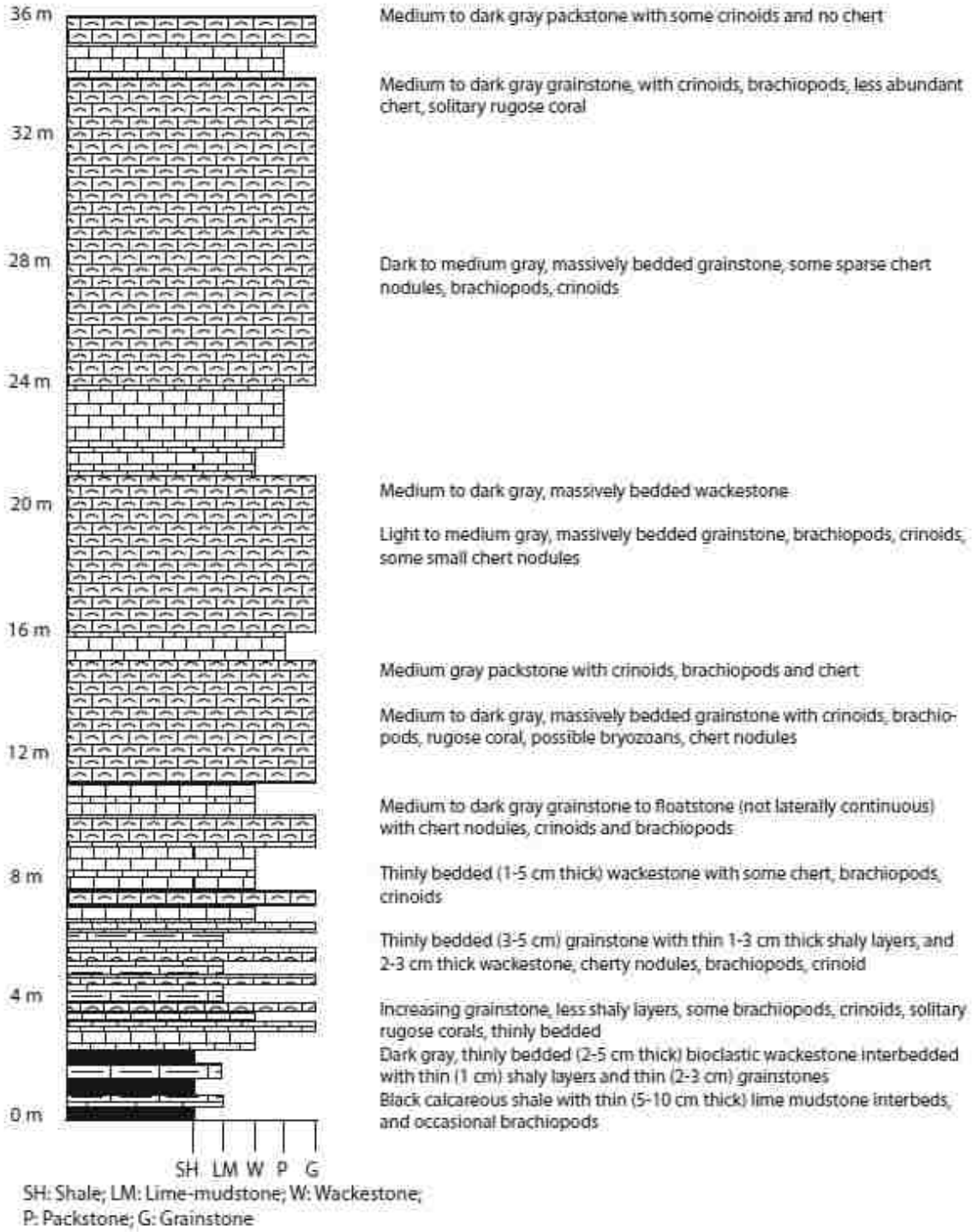

SH: Shale; LM: Lime-mudstone; W: Wackestone;
P: Packstone; G: Grainstone

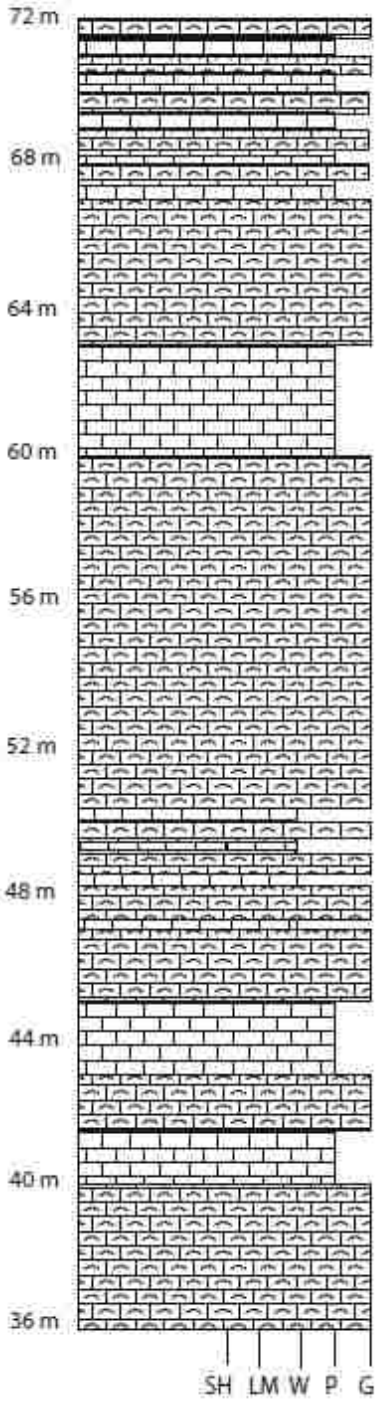

72-67: Mostly medium to light gray packstones with thin (2-10 cm thick) grainstones (medium gray), some chert nodules, some sparse brachiopods in cross-section.

66-63: Medium to light gray grainstone with some thin (1-10 cm thick) wackestone and packstone, some increasing chert nodules, recrystallization present, brachiopods getting sparse.

63-60: Medium to light gray massively bedded packstone with some chert nodules, brachiopods and crinoids.

60-58: Dark to medium gray grainstone, massively bedded, some chert nodules and chertification of fossils, crinoids, solitary rugose and tabulate corals, brachiopods.

57-54: Medium to dark gray, massively bedded grainstone with small discontinuous packstone/wackestone layers (5-10 cm thick), brachiopods, crinoids, solitary rugose corals.

54-52: Medium to dark gray grainstone with some small 5-10 cm thick packstones, increasing brachiopods, crinoids, solitary rugose coral, some tabulate coral and sparse chert.

52-45: Dark to medium gray, massively bedded grainstone with some small discontinuous packstones, brachiopods, tabulate coral, crinoids, very infrequent chert.

45-43: Dark to medium gray, massively bedded packstone with brachiopods and crinoids.

43-42: Light to medium gray, massively bedded grainstone, brachiopods, crinoids, tabulate corals.

42-38: Dark to medium gray grainstone to packstone, massively bedded, crinoids, brachiopods, solitary rugose corals, tabulate coral.

38-35: Medium to light gray grainstone with some chert nodules, thickly to massively bedded, crinoids, brachiopods, solitary rugose and tabulate colonial corals.

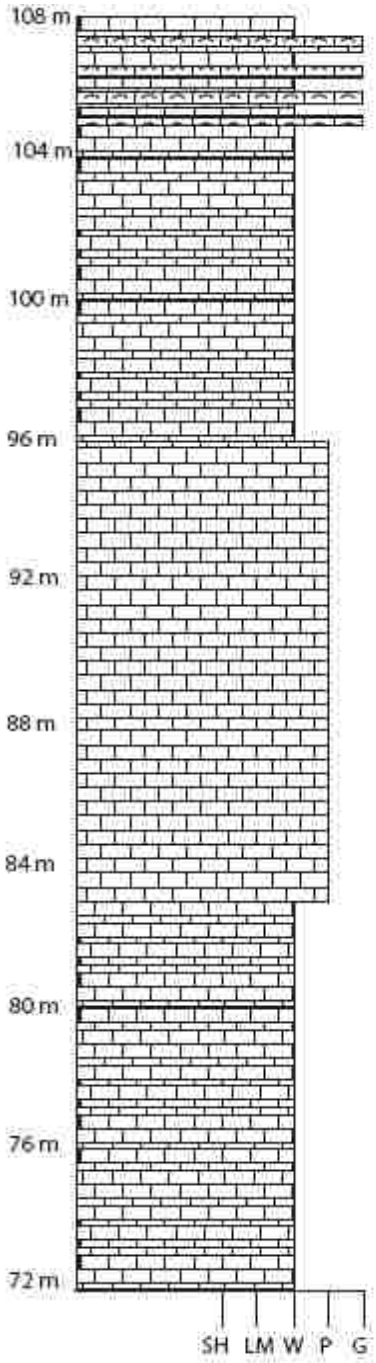

108-106: Dark to medium gray wackestone with thin discontinuous beds of dark gray grainstone 5-10 cm thick, crinoids, bioturbation, brachiopods, Zoophycos trails in wackestone.

105-103: Medium to dark gray wackestone with some chert, medium to thickly bedded (20-30 cm thick beds) bioturbated, crinoids, some brachiopods.

103-100: Thick cherty layer (5-15 cm thick) at 102.9m, medium gray wackestone with some brachiopods, microbial bedded cherts and crinoids.

98-96: Medium to light gray wackestone with some bedded cherts and some brachiopods and crinoids.

96-88: Medium to light gray packstone thickly-massively bedded with some increasing brachiopods since 87m, some bedded chert, crinoids.

88-83m: Light to medium gray packstone thickly bedded, some chert, crinoids, some sparse brachiopods.

83-80: Medium gray wackestone with microbial bedded cherts, no fossils, some recrystallization.

78-74: Medium gray thickly bedded wackestone with some dark gray, bedded (2-4 cm thick) chert, no fossils.

74-72: Medium to light gray thickly bedded wackestone with some chert, fossil free, some discontinuous 1-2 cm thick packstones and grainstones.

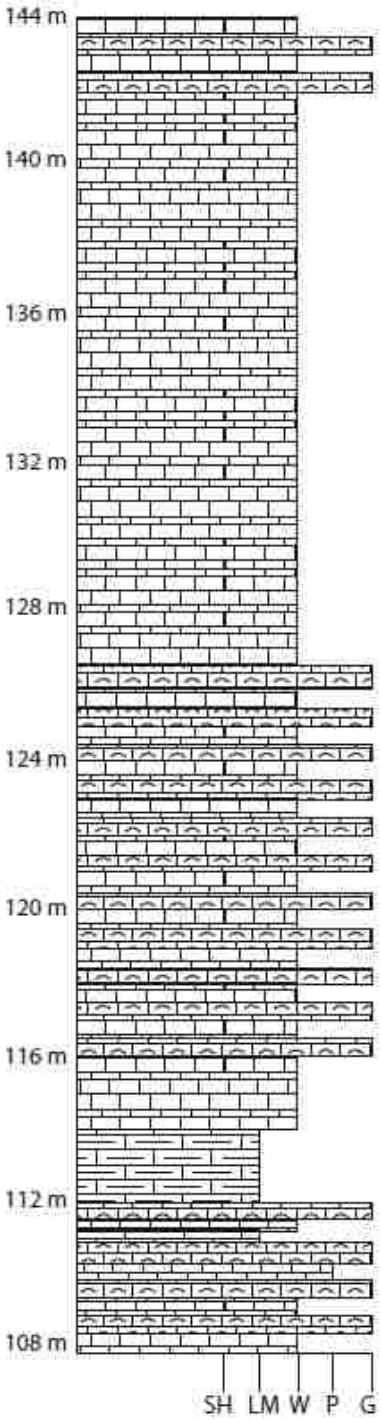

144-140: Alternating medium to dark gray 5-10 cm thick wackestone and grainstone with some chert and shaly partings, crinoids brachiopods, tabulate coral, bioturbation.

140-138: Medium to dark gray wackestone with 10-20 cm thick beds, crinoids, brachiopods, solitary rugose corals, some chert beds 1-5 cm thick

138-132: Dark gray 10-30 cm thick bedded wackestone with bioturbation, brachiopods, crinoids, some interbedded 1-10 cm thick chert beds.

132-126: Mainly dark to medium gray wackestone with 5-10 cm thick beds, bioturbation, tabulate and solitary rugose corals, brachiopods, crinoids, some sparse chert

126-124: Dark gray wackestone with 10-30 cm thick beds with interbedded 5-20 cm thick grainstones, bioturbated, some Zoophycos, brachiopods, crinoids and chert.

124-120: Highly bioturbated dark gray wackestone thinly bedded (3-10 cm thick beds) some laterally discontinuous grainstone beds with shaly partings, brachiopods, crinoids, solitary rugose corals.

120-116: Dark gray wackestone with 10-20 cm thick beds, bioturbated, some brachiopods, crinoids. Some dark gray grainstone interbeds (1-5 cm thick) with some shaly partings, crinoids, brachiopods, and solitary rugose coral.

114-112: Dark gray wackestone with 5-15 cm thick beds and 3-5 cm thick dark gray grainstones.

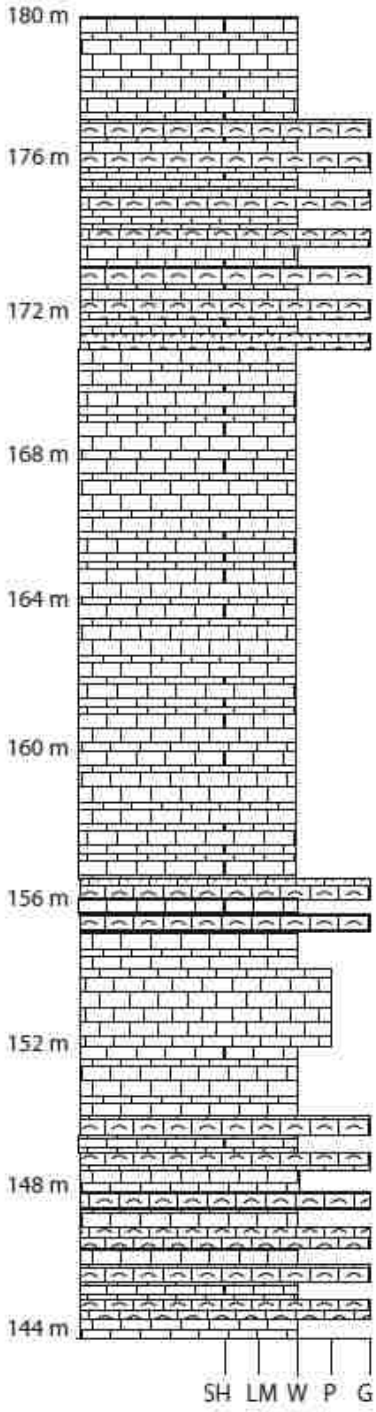

177-172: Dark gray 10-30 cm thick wackestones with 1-5 cm thick floatstones, tabulate coral bioherms, brachiopods, crinoids, solitary rugose corals, some chert nodules.

171: bioherm of tabulate coral.

170-168: Dark to medium gray wackestone with 5-20 cm thick beds some sparse chert nodules, brachiopods, tabulate and solitary rugose corals, crinoids, some small shaly partings.

168-166: Dark gray 15-20 cm thick wackestone with inconsistent chert nodules, brachiopods, crinoids, solitary rugose and tabulate corals, bryozoans, microbial coral mound, some bioturbation.

164-162: Dark gray wackestone with 10-20 cm thick beds, brachiopods, crinoids, solitary rugose coral, some tabulate coral, some bryozoans, bioturbation.

160-156: Dark gray wackestone 10-40 cm thick beds, some small chert nodules, abundant fossils including brachiopods, crinoids, solitary rugose corals, fenestrate bryozoans and some tabulate coral.

156-154: Dark gray wackestone grading into dark gray grainstone, all fossils in grainstone, crinoids, corals, bryozoans, brachiopods.

154-152: Dark gray (5-15 cm thick beds) packstone with some shaly partings crinoids, brachiopods, solitary rugose coral.

152-150: Dark gray medium bedded wackestone, some chert nodules, crinoids, brachiopods, solitary rugose coral.

150-146: Mostly dark to medium gray grainstone with some interbedded wackestone, 10-25 cm thick beds, brachiopods, crinoids, corals, some chert nodules.

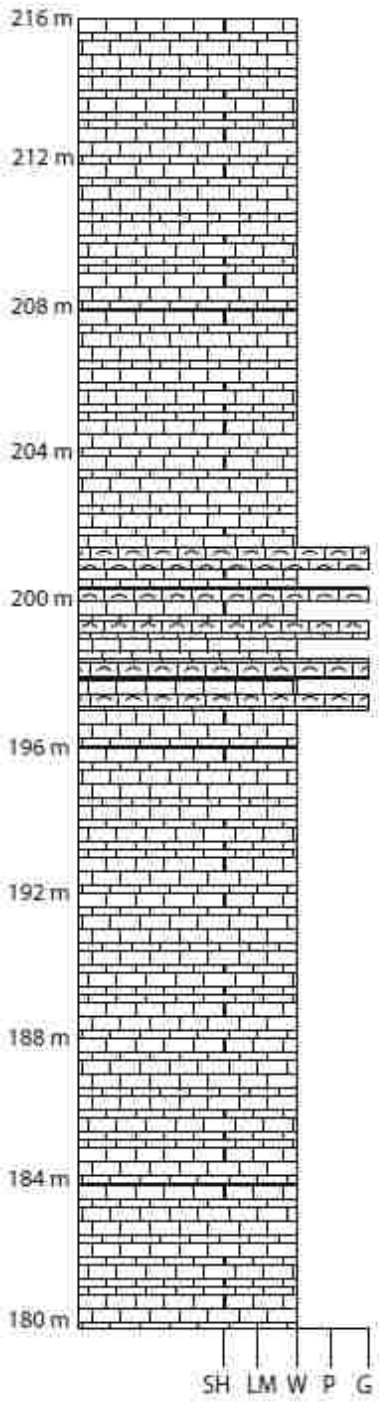

214-212: Dark gray wackestone 10-30 cm thick beds with increasing shaly partings, brachiopods, crinoids, solitary rugose corals, some bioturbation and very small chert nodules.

210-208: Dark to medium gray wackestone 10-20cm thick with some small 1-2 cm thick packstones, grainstones and shaly partings, brachiopods, crinoids, solitary rugose corals.

206-202: Dark to medium gray wackestone (10-30 cm thick beds) with smally shaly partings and 3-5 cm thick grainstone beds, brachiopods, crinoids and solitary rugose corals.

200-194: Dark gray wackestone
10-30 cm thick beds and some 3-5 cm thick grainstone layers, brachiopods, tabulate and solitary rugose corals, crinoids.

190-186: Dark gray wackestone 20-40 cm thick, with some chert nodules, brachiopods, fenestrate bryozoans, solitary rugose corals, tabulate coral.

184-178: Dark gray wackestone 15-40 cm thick beds, increasing chert, some smaller tabulate coral bioherms, bryozoans, brachiopods, solitary rugose coral, crinoids.

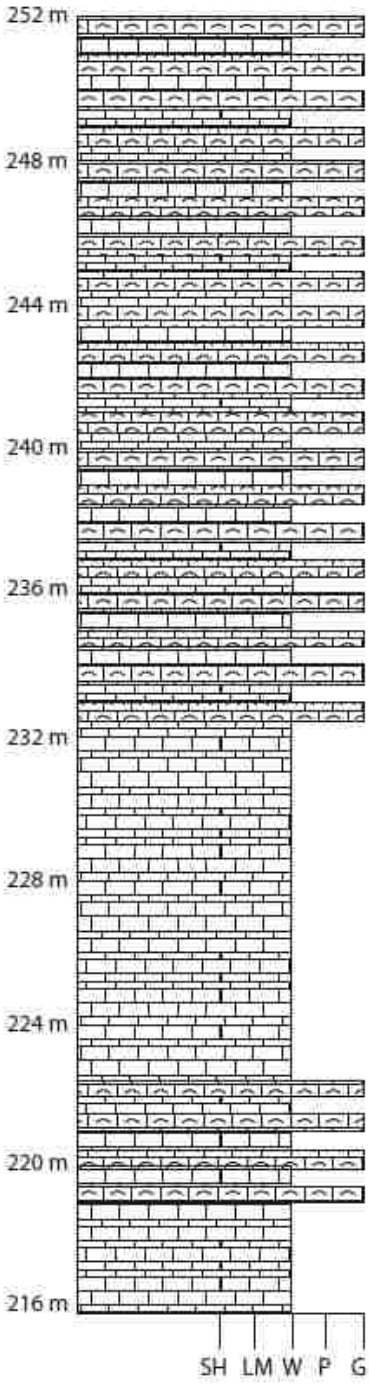

252-244: Dark gray wackestone thinly to medium bedded (10-30cm thick beds) with interbedded grainstones (3-10cm thick), some more prominent shaley partings and bioturbated layers (1-3cm thick).

240-232: Dark gray wackestone 10-30 cm thick with some interbedded 1-10cm thick grainstones, brachiopods, corals, some crinoids, solitary rugose corals, some inconsistent chert nodules, bioturbation, and shaley partings.

230-228: Medium to dark gray wackestone with thin (1-5cm) laterally discontinuous muddy to grainstone layers, some chert nodules, brachiopods, gastropods, solitary rugose and tabulate corals, some minor bioturbation.

226-224: Dark to medium gray wackestone with some intermittent shaly partings, brachiopods crinoids, solitary rugose corals and gastropods.

222-218: Dark gray wackestone 10-20 cm thick with some shaly partings and 3-5 cm thick grainstones, brachiopods, crinoids, tabulate coral bioherms, solitary rugose coral.

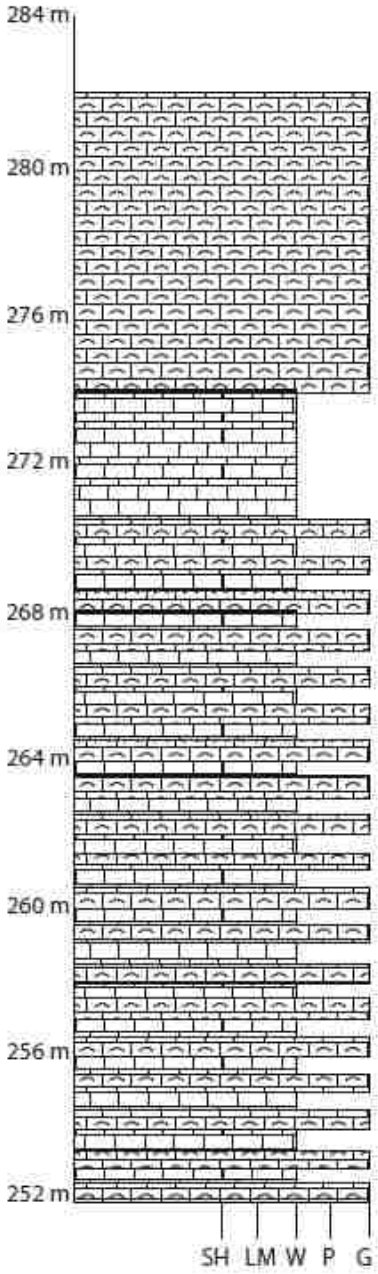

282-276: Medium gray grainstone to packstone with some chert nodules, brachiopods, crinoids, solitary rugose and tabulate coral.

276-274: Dark to medium gray wackestone with some interbedded grainstones not laterally continuous, solitary rugose corals, brachiopods, Zoophycos bioturbation, crinoids

270-264: Dark to medium gray wackestone medium-thinly bedded (10-30cm) with some 1-5 cm thick grainstones and some sparse chert nodules, brachiopods, solitary rugose corals, crinoids, bioturbation, Zoophycos.

264-260: Dark to medium gray wackestone with some thin grainstones and shaley partings 1-3 cm thick, some chert nodules, brachiopods, crinoids, solitary rugose corals, bryozoans, gastropods.

258-254: Dark to medium gray wackestone with some 1-3 cm thick grainstones and shaley partings, brachiopods, solitary rugose corals, gastropods, crinoids, chert nodules starting @ 255m.

Tungsten Gap section in Arrow Canyon detailed stratigraphic column

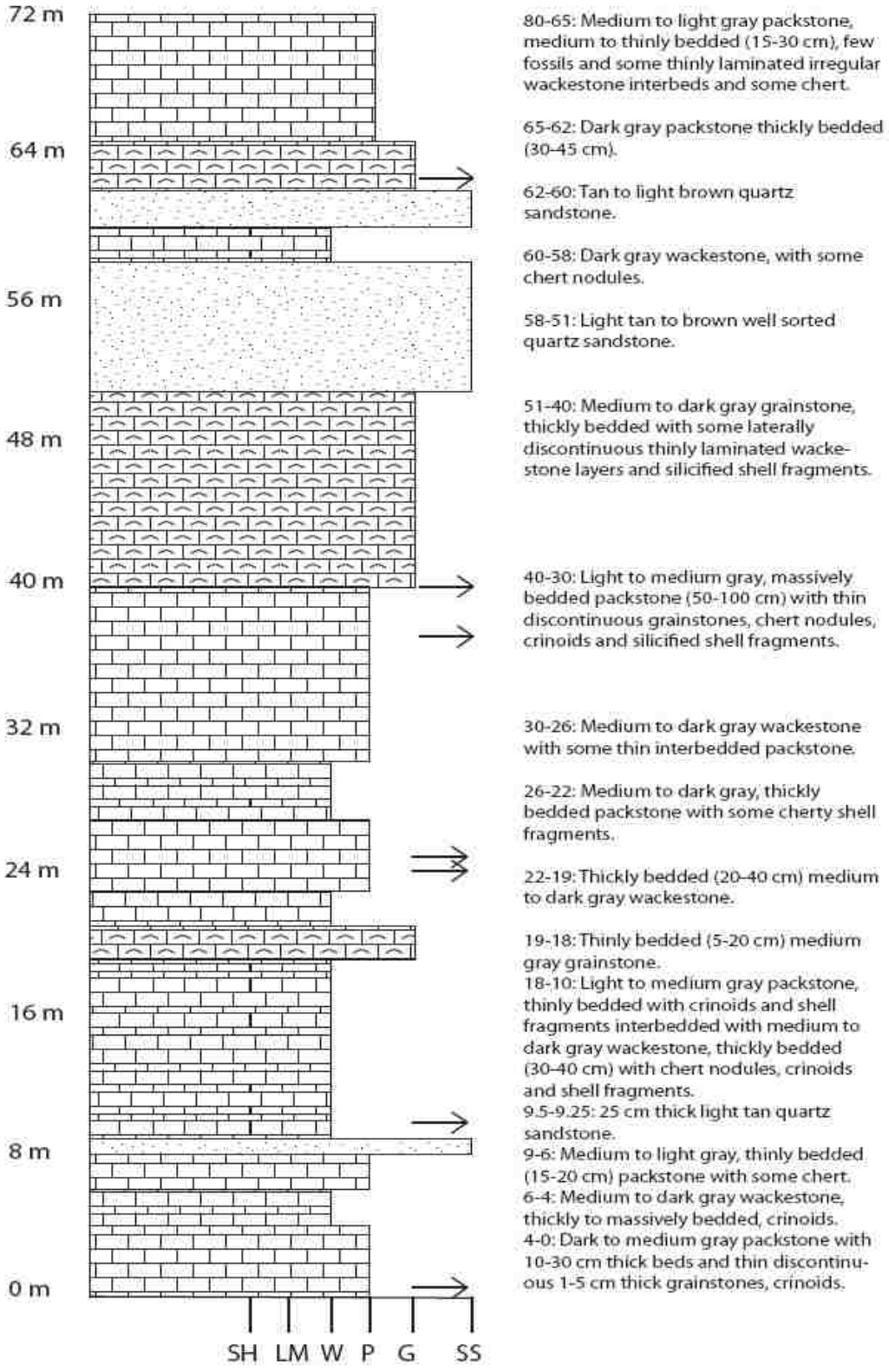

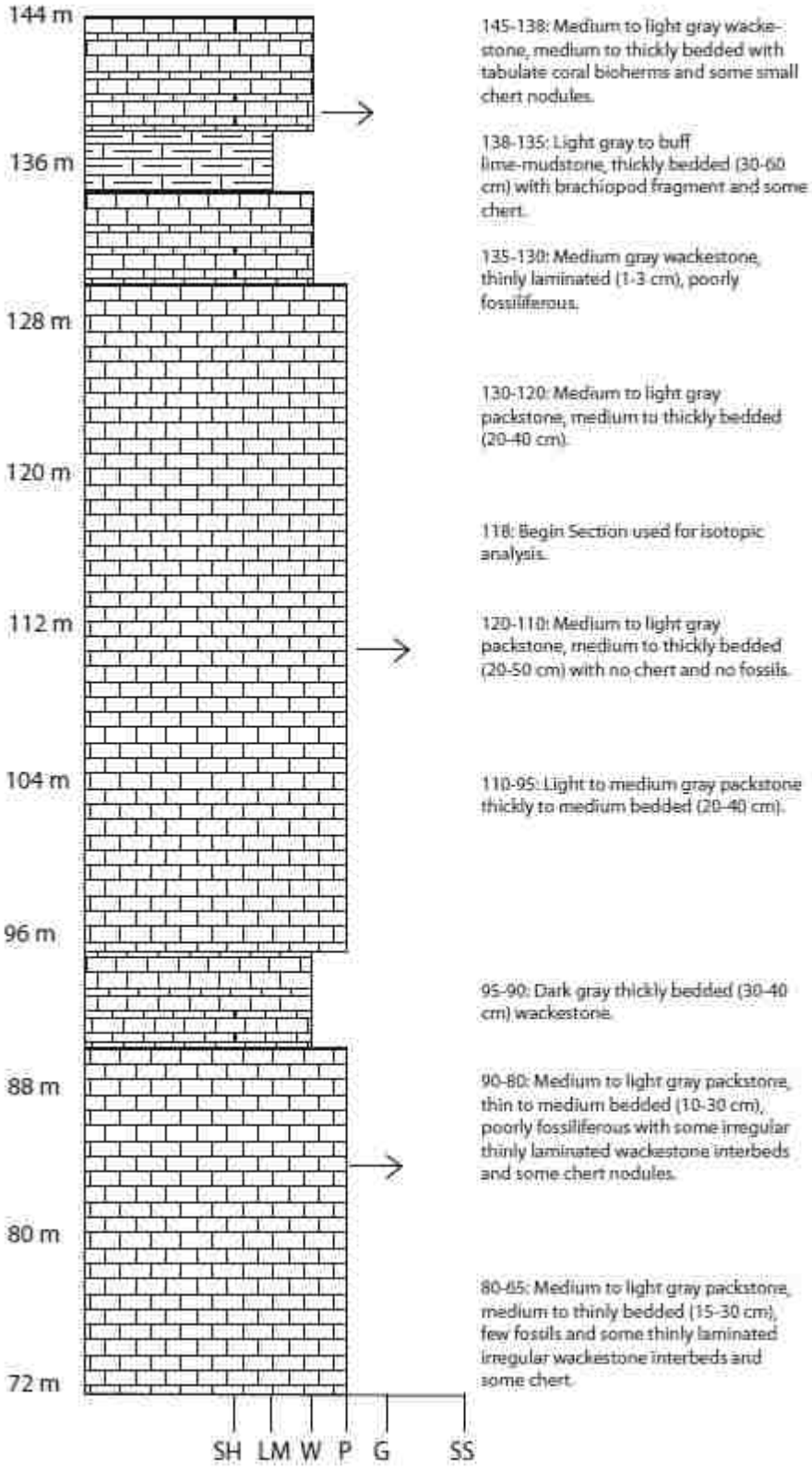
144 m
136 m
128 m
120 m
112 m
104 m
96 m
88 m
80 m
72 m
145-138: Medium to light gray wacke-stone, medium to thickly bedded with tabulate coral bioherms and some small chert nodules.
138-135: Light gray to buff lime-mudstone, thickly bedded (30-60 cm) with brachiopod fragment and some chert.
135-130: Medium gray wackestone, thinly laminated (1-3 cm), poorly fossiliferous.
130-120: Medium to light gray packstone, medium to thickly bedded (20-40 cm).
118: Begin Section used for isotopic analysis.
120-110: Medium to light gray packstone, medium to thickly bedded (20-50 cm) with no chert and no fossils.
110-95: Light to medium gray packstone thickly to medium bedded (20-40 cm).
95-90: Dark gray thickly bedded (30-40 cm) wackestone.
90-80: Medium to light gray packstone, thin to medium bedded (10-30 cm), poorly fossiliferous with some irregular thinly laminated wackestone interbeds and some chert nodules.
80-65: Medium to light gray packstone, medium to thinly bedded (15-30 cm), few fossils and some thinly laminated irregular wackestone interbeds and some chert.
SH LM W P G SS

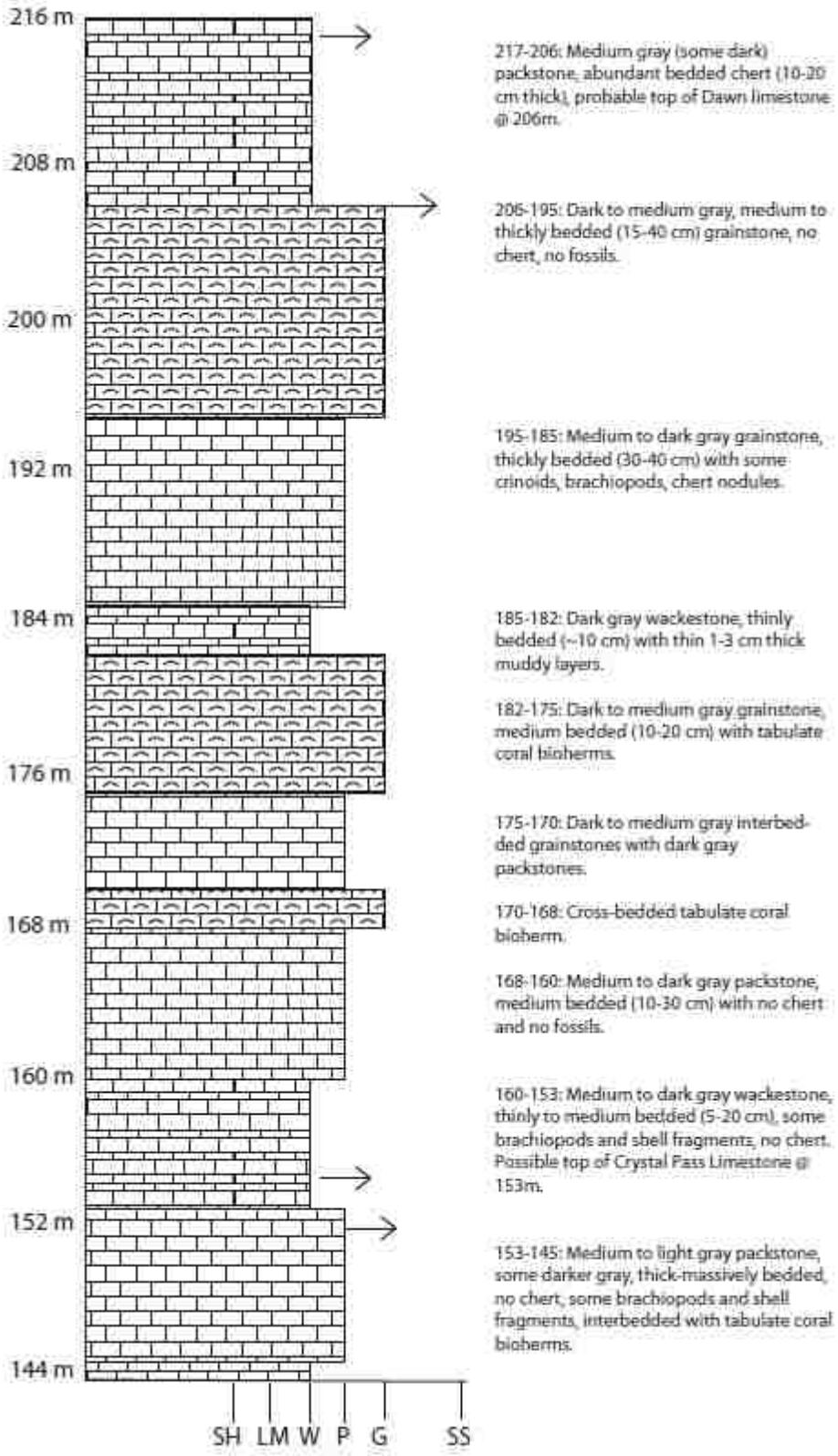
216 m
208 m
200 m
192 m
184 m
176 m
168 m
160 m
152 m
144 m
217-206: Medium gray (some dark) packstone, abundant bedded chert (10-20 cm thick), probable top of Dawn limestone @ 206m.
206-195: Dark to medium gray, medium to thickly bedded (15-40 cm) grainstone, no chert, no fossils.
195-185: Medium to dark gray grainstone, thickly bedded (30-40 cm) with some crinoids, brachiopods, chert nodules.
185-182: Dark gray wackestone, thinly bedded (~10 cm) with thin 1-3 cm thick muddy layers.
182-175: Dark to medium gray grainstone, medium bedded (10-20 cm) with tabulate coral bioherms.
175-170: Dark to medium gray interbedded grainstones with dark gray packstones.
170-168: Cross-bedded tabulate coral bioherm.
168-160: Medium to dark gray packstone, medium bedded (10-30 cm) with no chert and no fossils.
160-153: Medium to dark gray wackestone, thinly to medium bedded (5-20 cm), some brachiopods and shell fragments, no chert. Possible top of Crystal Pass Limestone @ 153m.
153-145: Medium to light gray packstone, some darker gray, thick-massively bedded, no chert, some brachiopods and shell fragments, interbedded with tabulate coral bioherms.
SH
LM
W
P
G
SS

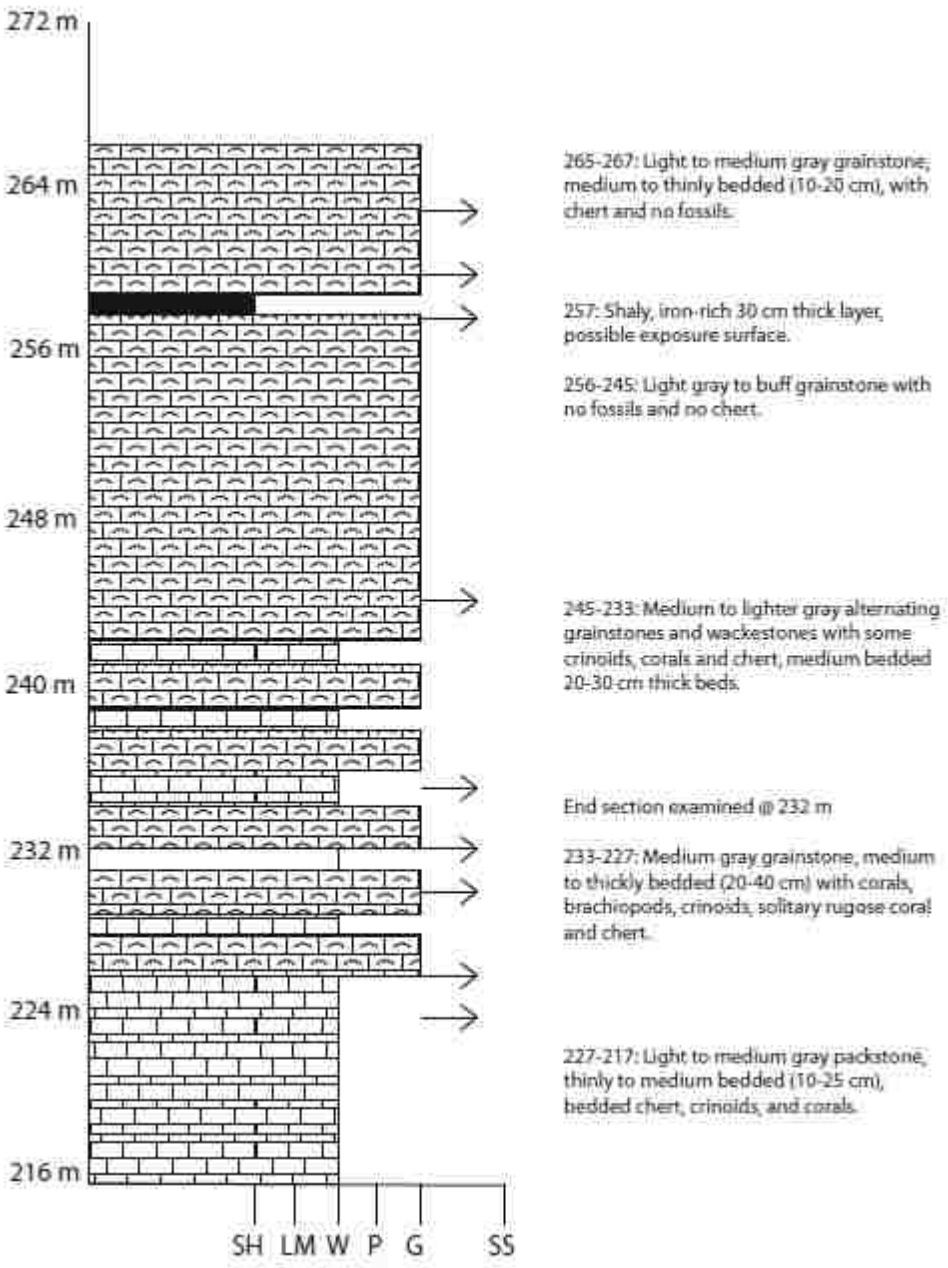
272 m
264 m
256 m
248 m
240 m
232 m
224 m
216 m
SH LM W P G SS
265-267: Light to medium gray grainstone, medium to thinly bedded (10-20 cm), with chert and no fossils.
257: Shaly, iron-rich 30 cm thick layer, possible exposure surface.
256-245: Light gray to buff grainstone with no fossils and no chert.
245-233: Medium to lighter gray alternating grainstones and wackestones with some crinoids, corals and chert, medium bedded 20-30 cm thick beds.
End section examined @ 232 m
233-227: Medium gray grainstone, medium to thickly bedded (20-40 cm) with corals, brachiopods, crinoids, solitary rugose coral and chert.
227-217: Light to medium gray packstone, thinly to medium bedded (10-25 cm), bedded chert, crinoids, and corals.

APPENDIX IV

Location Maps

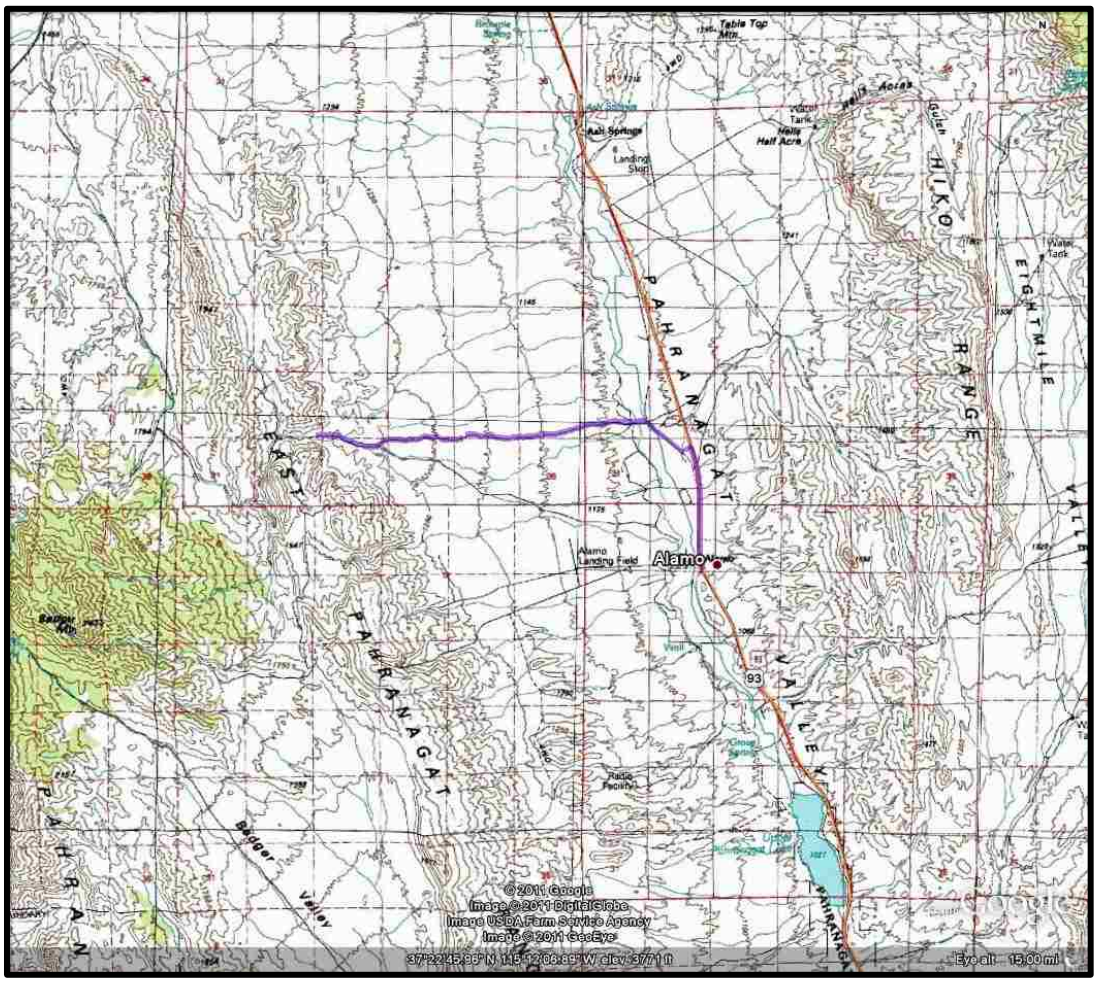

From Alamo, NV take Hwy 93N for about 2 miles then turn left (west) onto Curtis Canyon Road (Purple). Continue on Curtis Canyon Road for about 5 miles arriving at the coordinates: 37° 23.4585'N, 115° 15.985'W.

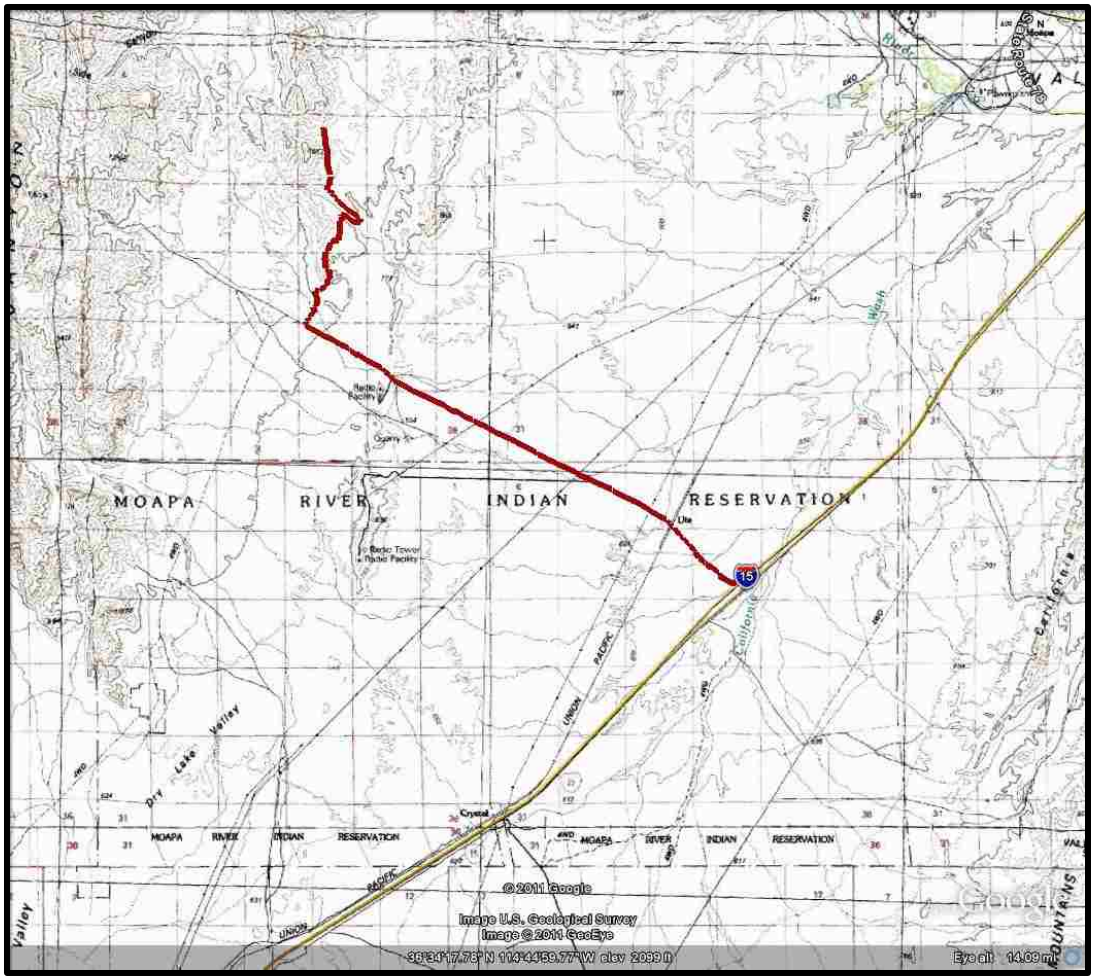

Take exit 80 on I-15N and turn left (west) continue on dirt road for about 8 miles. Follow dirt road (Red) toward right for 3.3 miles coming to the end of the road. Continue on foot to 36° 38.852'N, 114° 48.514'W.

REFERENCES

Allan, J.R., and Matthews, R.K., 1982, Isotope signatures associated with early meteoric diagenesis: Sedimentology, v. 29, p. 797-817.

Alley, R.B., and Cuffey, K.M., 2001, Oxygen- and hydrogen-isotopic ratios of water in precipitation: Beyond paleothermometry: Reviews in Mineralogy and Geochemistry, v. 43, p. 527-553.

Arthur, M.A., Dean, W.E., Pratt, L.M., 1988, Geochemical and climatic effects of increased marine organic carbon burial at the Cenomanian/Turonian boundary: Nature, v. 335, p. 714-717.

Banner, J.L., and Hanson, G.N., 1990, Calculation of simultaneous isotopic and trace element variations during water-rock interaction with applications to carbonate diagenesis: Geochimica et Cosmochimica Acta, v. 54, p. 3123-3137.

Blakey, R., 2010, NAU Geology: http://jan.ucc.nau.edu/~rcb7/RCB.html

Brand, U., 2004, Carbon, oxygen and strontium isotopes in Paleozoic carbonate components: an evaluation of original seawater-chemistry proxies: Chemical Geology, v. 204, p. 23-44.

Bruckschen, P., and Veizer, J., 1997, Oxygen and carbon isotopic composition of Dinantian brachiopods: Paleoenvironmental implications for the Lower Carboniferous of western Europe: Palaeogeography, Palaeoclimatology, Palaeoecology, v. 132, p. 243-264.

Budai, J.M., Lohmann, K.C., Wilson, J.L., 1987, Dolomitization of the Madison Group, Wyoming and Utah overthrust belt: American Assocation of Petroleum Geologists Bulletin, v. 71, p. 909-924.

Buggisch, W., Joachimski, M.M., Sevastopulo, G., Morrow, J.R., 2008, Mississippian $\delta^{13}C_{carb}$ and conodont apatite $\delta^{18}O$ records – Their relation to the Late Palaeozoic Glaciation: Palaeogeography, Palaeoclimatology, Palaeoecology, v. 268, p. 273-292.

Carpenter, S.J., and Lohmann, K.C., 1997, Carbon isotope ratios of Phanerozoic marine cements: Reevaluating the global carbon and sulfur systems: Geochimica et Cosmochimica Acta, v. 61, p. 4831-4846.

Caputo, M.V., 1985, Late Devonian glaciation in South America: Palaeogeography, Palaeoclimatology, Palaeoecology, v. 51, p. 291-317.

Cohen, A.S., Coe, A.L., Kemp, D.B., 2007, The Late Palaeocene-Early Eocene and Toarcian (Early Jurassic) carbon isotope excursions: a comparison of their time scales, associated environmental changes, causes and consequences: Journal of the Geological Society, London, v. 164, p. 1093-1108.

Conway, N.M., Kennicut, M.C., Van Dover, C.L., 1994, Stable isotopes in the study of marine chemosynthetic-based food webs. In: Lajtha, K., Michener, R. (Eds.), Stable Isotopes in Ecology and Environmental Science, Blackwell Scientific Publications, Oxford, pp. 158-186.

Cramer, B.D., Saltzman, M.R., 2007, Early Silurian paired $\delta^{13}C_{carb}$ and $\delta^{13}C_{org}$ analyses from the Midcontinent of North America: implications for paleoceanography

and paleoclimate: Palaeogeography, Palaeoclimatology, Palaeoecology, v. 256, p. 195-203.

Denison, R.E., Koepnick, R.B., Fletcher, A., Howell, M.W., Calloway, W.S., 1994, Criteria for the retention of original seawater $^{87}Sr/^{86}Sr$ in ancient limestones: Chemical Geology, v. 112, p. 132-143.

Derry, L.A., 2010, On the significance of $\delta^{13}C$ correlations in ancient sediments: Earth and Planetary Science Letters, v. 296, p. 497-501.

Dickens, G.R., O'Neil, J.R., Rea, D.K., Owen, R.M., 1995, Dissociation of oceanic methane hydrate as a cause of the carbon isotope excursion at the end of the Paleocene: Paleoceanography, v. 10, p. 965-971.

Dickinson, W.R., 2006, Geotectonic evolution of the Great Basin: Geosphere, v. 2, p. 353-368.

Falkowski, P., Scholes, R.J., Boyle, E., Canadell, J., Canfield, D., Elser, J., Gruber, N., Hibbard, K., Högberg, P., Linder, S., Mackenzie, F.T., Moore III, B., Pederson, T., Resenthal, Y., Seitzinger, S., Smetacek, V., Steffen, W., 2000, The Global Carbon Cycle: A Test of Our Knowledge of Earth as a System: Science, v. 290, p. 291-296.

Garzanti, E., Sciunnach, D., 1997, Early Carboniferous onset of Gondwanian glaciation and Neo-tethyan rifting in South Tibet: Earth and Planetary Science Letters, v. 148, p. 359-365.

Giles, K.A., 1996, Tectonically forced retrogradation of the Lower Mississippian Joana Limestone, Nevada and Utah: In Longman, M.W., and Sonnenfeld, M.D. (Eds.), Paleozoic systems of the Rocky Mountain Region: Denver, Colorado, Rocky

Mountain Section SEPM, p. 145-164.

Giles, K.A., and Dickinson, W.R., 1995, The interplay of eustasy and lithospheric flexure in forming stratigraphic sequences in foreland settings: An example from the Antler foreland, Nevada and Utah. In Dorobek, S.L., and Ross, G.M. (Eds.), Stratigraphic Evolution of Foreland Basins: Society for Sedimentary Geology Special Publication, 52, p. 187-211.

Goebel, K.A., 1991, Interpretation of the Lower Mississippian Joana Limestone and implications for the Antler orogenic system (Ph.D. thesis): Tucson, University of Arizona, 222 p.

González-Bonorino, G., 1992, Carboniferous glaciation in Gondwana. Evidence for grounded marine ice and continental glaciation in southwestern Argentina: Palaeogeography, Palaeoclimatology, Palaeoecology, v. 91, p. 363-375.

Hansen, M.W., and Carozzi, A.V., 1974, Carbonate microfacies of the Monte Cristo Group (Mississippian), Arrow Canyon Range, Clark County, Nevada: The Wyoming Geological Association Earth Science Bulletin, v. 7, p. 13-54.

Harris, D., Horwath, W.R., van Kessel, C., 2001, Acid fumigation of soils to remove carbonates prior to total organic carbon or Carbon-13 isotopic analysis: Soil Science Society of America Journal, v. 65, p. 1853-1856.

Hayes, J.M., Kaplan, I.R., Wedeking, K.W., 1983, Precambrian organic geochemistry, preservation of the record. In Schopf, J.W. (Ed.), The Earth's Earliest Biosphere: Its origin and evolution: Princeton, N.J., Princeton University Press, p. 93-134.

Hayes, J.M., Popp, B.N., Takigiku, R., Johnson, M.W., 1989, An isotopic study of

biogeochemical relationships between carbonates and organic carbon in the Greenhorn Formation: Geochimica et Cosmochimica Acta, v. 53, p. 2961-2972.

Hayes, J.M., Strauss, H., Kaufman, A.J., 1999, The abundance of ^{13}C in marine organic matter and isotopic fractionation in the global biogeochemical cycle of carbon during the past 800 Ma: Chemical Geology, v. 161, p. 103-125.

Hedges, J.L., and Stern, J.H., 1984, Carbon and nitrogen determination of carbonate-containing solids: Limnology and Oceanography, v. 29, p. 657-663.

Hesselbo, S.P., Gröcke, D.R., Jenkyns, H.C., Bjerrum, C.J., Farrimond, P., Morgans Bell, H.S., Green, O.R., 2000, Massive dissociation of gas hydrate during a Jurassic oceanic anoxic event: Nature, v. 406, p. 392-395.

Hesselbo, S.P., Jenkyns, H.C., Duarte, L.V., Oliveira, L.C.V., 2007, Carbon-isotope record of the Early Jurassic (Toarcian) Oceanic Anoxic Event from fossil wood and marine carbonate (Lusitanian Basin, Portugal): Earth and Planetary Science Letters, v. 253, p. 455-470.

Hoefs, J., 2009, Stable Isotope Geochemistry: 6th Edition, Springer, XII, 288 p.

Holland, H.D., Lazar, B., McCaffrey, M., 1986, Evolution of the atmosphere and oceans: Nature, v. 320, p. 27-33.

Hollander, D.J., and Smith, M.A., 2001, Microbially mediated carbon cycling as a control on the $\delta^{13}C$ of sedimentary carbon in eutrophic Lake Mendota (USA): new models for interpreting isotopic excursions in the sedimentary record: Geochemica et Cosmochimica Acta, v. 65, p. 4321-4337.

Jenkyns, H.C., 2003, Evidence for rapid climate change in the Mesozoic-Palaeogene greenhouse world: Phil. Trans. Royal Society of London, v. 361, p. 1885-1916.

Kaufman, A.J., and Knoll, A.H., 1995, Neoproterozoic variations in the C-isotopic composition of seawater; stratigraphic and biogeochemical implications: Precambrian Research, v. 73, p. 27-49.

Kemp, D.B., Coe, A.J., Cohen, A.S., Schwark, L., 2005, Astronomical pacing of methane release in the Early Jurassic Period: Nature, v. 437, p. 396-399.

Knauth, L.P., and Kennedy, M.J., 2009, The late Precambrian greening of the Earth: Nature, v. 460, p. 728-732.

Knoll, A.H., Hayes, J.M., Kaufman, A.J., Swett, K., Lambert, I.B., 1986, Secular variation in carbon isotope ratios from upper Proterozoic successions of Svalbard and East Greenland: Nature, v. 321, p. 832-838.

Kump, L.R., Arthur, M.A., 1999, Interpreting carbon-isotope excursions, carbonates and organic matter: Chemical Geology, v. 161, p. 181-198.

Langenheim, R.L., Schulmeister, M.K., 1987, Virgin River Gorge; Boundary between the Colorado Plateau and the Great Basin in northwestern Arizona: Geological Society of America Centennial Field Guide—Cordilleran Section, p. 43-48.

Magaritz, M., Krishnamurthy, R.V., Holser, W.T., 1992, Parallel trends in organic and inorganic carbon isotopes across the Permian/Triassic Boundary: American Journal of Science, v. 292, p. 727-729.

Mii, H., Grossman, E.L., Yancey, T.E., 1999, Carboniferous isotope stratigraphies of North America: implications for Carboniferous paleoceanography and Mississippian glaciation: Geological Society of America Bulletin, v. 111, p. 960-973.

Pagani, M., Caldiera, K., Archer, D., Zachos, J.C., 2006, An ancient carbon mystery: Nature, v. 314, p. 1556-1557.

Pierce, R.W., 1969, Ultrastructure and biostratigraphy of the conodonts of the Monte Cristo Group, Arrow Canyon Range, Clark County Nevada (Ph.D. thesis): University of Illinois, 113 pp.

Pierce, R.W., and Langenheim, R.L., Jr., 1974, Platform conodonts of the Monte Cristo Group, Mississippian, Arrow Canyon Range, Clark County, Nevada: Journal of Paleontology, v. 48, p. 149-169.

Popp, B.N., Anderson, T.F., Sandberg, P.A., 1986, Brachiopods as indicators of original isotopic compositions in some Paleozoic limestones: Geological Society of America Bulletin, v. 97, p. 1262-1269.

Popp, B.N., Laws, E.A., Bidigare, R.R., Dore, J.E., Hanson, K.L., Wakeham, S.G., 1998, Effect of phytoplankton cell geometry on carbon isotopic fractionation: Geochemica et Cosmochimica Acta, v. 62, p. 69-77.

Raven, J.A., Johnston, A.M., Kubler, J.E., Korb, R.E., McInroy, S.G., Handley, L.L., Scrimgeor, C.M., Walker, D.I., Beardall, J., Vanderklift, M., Frederiksen, J., Dunton, K.H., 2002, Mechanistic interpretation of carbon isotope discrimination by marine macroalgae and seagrasses: Functional Plant Biology, v. 29, p. 355-378.

Reso, A., 1963, Composite columnar section of exposed Paleozoic and Cenozoic rocks in the Pahranagat Range, Lincoln County, Nevada: Geological Society of America Bulletin, v. 74, p. 901-918.

Rothman, D.H., Hayes, J.M., Summons, R.E., 2003, Dynamics of the Neoproterozoic

carbon cycle: PNAS, v. 100, p. 8124-8129.

Ruby, E.G., Jannasch, H.W., Deuser, W.G., 1987, Fractionation of stable carbon isotopes during chemoautotrophic growth of sulfur-oxidizing bacteria: Applications in Environmental Microbiology, v. 53, p. 1940-1943.

Ruddiman, W.F., 2001, Earth's Climate Past and Future: W.H. Freeman, New York, 465 p.

Saltzman, M.R., Gonzalez, L.A., Lohmann, K.C., 2000, Earliest Carboniferous cooling step triggered by the Antler Orogeny?: Geology, v. 28, p. 347-350.

Saltzman, M.R., 2002, Carbon and oxygen isotope stratigraphy of the Lower Mississippian (Kinderhookian-early Osagean), western United States: Implications for seawater chemistry and glaciation: Geological Society of America, v. 114, p. 96-108.

Saltzman, M.R., 2003a, Late Paleozoic ice age: oceanic gateway or pCO_2?: Geology, v. 31, p. 151-154.

Saltzman, M.R., 2003b, Organic carbon burial and phosphogenesis in the Antler Foreland Basin: an out of phase relationship during the Lower Mississippian: Journal of Sedimentary Research, v. 73, p. 844-855.

Saltzman, M.R., Groessens, E., Zhuravlev, A.V., 2004, Carbon cycle models based on extreme changes in $\delta^{13}C$: an example from the lower Mississippian: Palaeogeography, Palaeoclimatology, Palaeoecology, v. 213, p. 359-377.

Saltzman, M.R., 2005, Phosphorus, nitrogen, and the redox evolution of the Paleozoic oceans: Geology, v. 33, p. 573-576.

Scotese, C.R., and McKerrow, W.S., 1990, Revised world maps and introduction:

Palaeozoic Palaeogeography and Biogeography: Geological Society Memoir 12, p. 1-21.

Singler, C.S., 1987, Carbonate petrology and conodont biostratigraphy of a Mississippian carbonate unit, East Pahranagat Range, Lincoln County, Nevada [M.S. Thesis]: Pullman, Washington State University, 107 p.

Sluijs, A., Brinkhuis, H., Schouten, S., Bohaty, S.M., John, C.M., Zachos, J.C., Reichart, G.J., Sinninghe Damasté, J.S., Crouch, E.M., Dickens, G.R., 2007, Environmental precursors to rapid light carbon injection at the Palaeocene/Eocene boundary: Nature, v. 450, p. 1218-1221.

Soreghan, G.S., Soreghan, M.J., Poulson, C.J., Young, R.A., Eble, C.F., Sweet, D.E., Davogustto, O.C., 2008, Anomalous cold in the Pangean tropics: Geology, v. 36, p. 659-662.

Speed, R.C., and Sleep, N.H., 1982, Antler orogeny and foreland basin: A model: Geological Society of America Bulletin, v. 93, p. 851-828.

Streel, M., Caputo, M.V., Loboziak, S., Melo, J.H.G., 2000, Late Frasnian-Famennian Climates based on palynomorph analyses and the question of the Late Devonian Glaciations: Earth Science Review, v. 52, p. 121-173.

Summons, R.E., Jahnke, L.L., Roksandic, Z., 1994, Carbon isotope fractionation in lipids from methanotrophic bacteria: relevance for interpretations of the geochemical record of biomarkers: Geochemica et Cosmochimica Acta, v. 58, p. 2853-2863.

Wang, K., Geldsetzer, H.H.J., Krouse, H.R., 1994, Permian-Triassic extinction: organic $\delta^{13}C$ evidence from British Columbia, Canada: Geology, v. 22, p. 580-584.

Ward, P.D., Botha, J., Buick, R., De Kock, M.O., Erwin, D.H., Garrison, G.H.,

Kirschvink, J.L., Smith, R., 2005, Abrupt and gradual extinction among Late Permian land vertebrates in the Karoo Basin, South Africa: Nature, v. 307, p. 709-714.

Young, S.A., Saltzman, M.R., Bergström, S.M., Leslie, S.A., Xu, C., 2008, Paired $\delta^{13}C_{carb}$ and $\delta^{13}C_{org}$ records of Upper Ordovician (Sandbian-Katian) carbonates in North America and China: implications for paleoceanographic change: Paleogeography, Palaeoclimatology, Palaeoecology, v. 270, p. 166-178.

VITA

Graduate College
University of Nevada, Las Vegas

Robert Alan Henry

Degrees:

Bachelor of Arts, Geology, 2007
Hartwick College

Thesis Title: Paired $\delta^{13}C_{carb}$ and $\delta^{13}C_{org}$, and $\delta^{18}O$ study across the Lower Mississippian positive carbon isotope excursion, Southeastern Nevada, USA

Thesis Examination Committee

Chairperson, Ganqing Jiang, Ph. D.
Committee Member, Stephen Rowland, Ph. D.
Committee Member, Margaret Rees, Ph. D.
Graduate Faculty Representative, Brian Hedlund, Ph. D.